

Topical Review

Angle-resolved photoemission spectroscopy studies of metallic surface and interface states of oxide insulators

Nicholas C Plumb¹  and Milan Radović^{1,2}

¹ Swiss Light Source, Paul Scherrer Institut, CH-5232 Villigen PSI, Switzerland

² SwissFEL, Paul Scherrer Institut, CH-5232 Villigen PSI, Switzerland

E-mail: nicholas.plumb@psi.ch and milan.radovic@psi.ch

Received 29 January 2016, revised 22 May 2017

Accepted for publication 1 August 2017

Published 28 September 2017



Abstract

Over the last decade, conducting states embedded in insulating transition metal oxides (TMOs) have served as gateways to discovering and probing surprising phenomena that can emerge in complex oxides, while also opening opportunities for engineering advanced devices. These states are commonly realized at thin film interfaces, such as the well-known case of LaAlO₃ (LAO) grown on SrTiO₃ (STO). In recent years, the use of angle-resolved photoemission spectroscopy (ARPES) to investigate the *k*-space electronic structure of such materials led to the discovery that metallic states can also be formed on the bare surfaces of certain TMOs.

In this topical review, we report on recent studies of low-dimensional metallic states confined at insulating oxide surfaces and interfaces as seen from the perspective of ARPES, which provides a direct view of the occupied band structure. While offering a fairly broad survey of progress in the field, we draw particular attention to STO, whose surface is so far the best-studied, and whose electronic structure is probably of the most immediate interest, given the ubiquitous use of STO substrates as the basis for conducting oxide interfaces. The ARPES studies provide crucial insights into the electronic band structure, orbital character, dimensionality/confinement, spin structure, and collective excitations in STO surfaces and related oxide surface/interface systems. The obtained knowledge increases our understanding of these complex materials and gives new perspectives on how to manipulate their properties.

Keywords: angle-resolved photoemission spectroscopy, transition metal oxides, two-dimensional electron gas, surfaces and interfaces, electronic structure

(Some figures may appear in colour only in the online journal)



Original content from this work may be used under the terms of the [Creative Commons Attribution 3.0 licence](https://creativecommons.org/licenses/by/3.0/). Any further distribution of this work must maintain attribution to the author(s) and the title of the work, journal citation and DOI.

1. Introduction

1.1. Motivation

Understanding the complex behaviors exhibited by transition metal oxides has presented condensed matter physics with some of its greatest contemporary challenges. Yet given the wide array of exotic and potentially useful properties exhibited by these materials—e.g. high-temperature superconductivity, colossal magnetoresistance, wide-ranging magnetically ordered states, metal-insulator transitions, ferroelectricity, and multiferroicity—the potential benefits for science, technology, and society are enormous.

The rich physics of TMOs stems from the non-negligible electron correlations inherent to d orbital systems, combined with complex couplings arising between the charge, orbital, spin, and lattice degrees of freedom. Surfaces, interfaces, and heterostructures are particularly appealing arenas for disentangling the interconnected factors at play in TMOs, with the added benefit that such fabricated systems may also function as platforms for oxide-based electronics and spintronics. The realization of a high-mobility conducting interface between the transition metal oxide insulators SrTiO_3 and LaAlO_3 [1] is widely credited with inspiring significant research into oxide interface applications while highlighting unique opportunities for investigating TMOs by tuning parameters such as strain, dimensionality, and carrier density, which are often difficult to manipulate in bulk crystals. Conducting interface states are now realized in numerous TMO interfaces that by-and-large share a common trait: they are based on SrTiO_3 [2–5]. More recently, the discoveries of metallic surface states on bare STO and a few other closely related compounds underscore the vital role played by these materials in hosting low-dimensional metals, while giving a new window into the mechanisms behind their intriguing behaviors.

Most of our understanding regarding these surface states has been obtained from the technique of ARPES, which gives a uniquely direct and powerful view of electronic structure and many-body interactions in momentum space. In fact, as will be discussed, ARPES is driving the realization of these surfaces both figuratively and, in many cases, literally, due to effects of the incident photon beam, which themselves give insights into the physics of such systems and the role of defects in manipulating the electronic properties. At the same time, much progress has been made in applying ARPES, which is famously surface-sensitive, to buried metallic oxide interfaces systems, thanks to experiments performed at resonant photon energies.

This topical review will summarize progress in the investigation of metallic surface and interface states embedded on/ in insulating TMOs, starting from the $\text{STO}(001)$ surface and extending to LAO/STO , with some additional connections to other closely related systems (e.g. TiO_2 and KTaO_3). The article is organized as follows: the remainder of section 1 introduces background information on STO bulk, surface, and interface properties. Section 2 provides a brief introduction to the ARPES technique. Section 3 gives an overview of the ARPES band structure measurements performed on STO

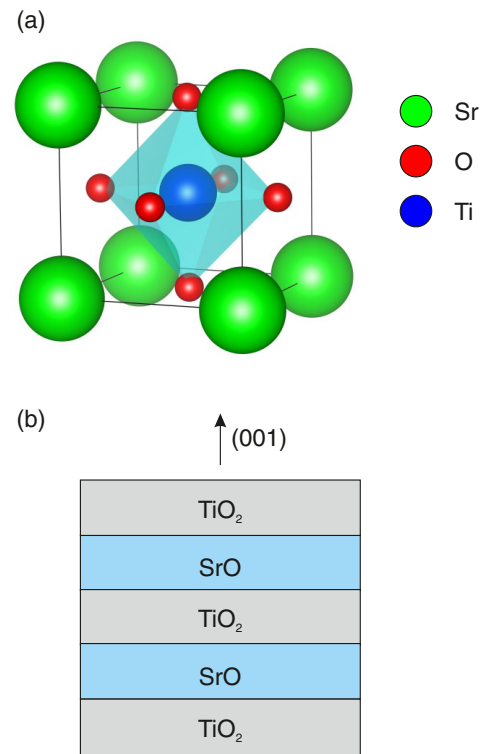


Figure 1. (a) Unit cell of cubic SrTiO_3 . (b) Stacking of the TiO_2 and SrO planes along the (001) direction.

surfaces, LAO/STO interfaces, and some related materials, as well as spin-resolved ARPES measurements of $\text{STO}(001)$. Section 4 discusses the observed signatures of electron-phonon coupling and polarons. Section 5 examines photoinduced changes seen during the ARPES experiments, which can help address the origins of surface/interface metallicity in these systems. We conclude with some brief final remarks in section 6.

1.2. Background on STO

1.2.1. Atomic structure. STO crystallizes in the cubic perovskite structure with lattice constant $a = 3.905 \text{ \AA}$. The unit cell, shown in figure 1(a), consists of a TiO_6 octahedron with Sr atoms situated at the corners of the cube. In the (001) direction, which is the most widely used surface for STO-based interfaces and heterostructures, the structure can be viewed as an alternating sequence of formally nonpolar SrO and TiO_2 planes (figure 1(b)). By contrast, the (011) and (111) directions correspond to $(\text{SrTiO})^{4+}/(\text{O}_2)^{4-}$ and $(\text{SrO}_3)^{4-}/\text{Ti}^{4+}$ polar layer stackings, respectively. STO is in the cubic $Pm\bar{3}m$ phase at high temperature and undergoes a phase transition below about 110 K to a slightly tetragonal structure with a reported ratio of the lattice constants $c/a = 1.00056$ [6]. Tetragonal domains persist in the surface region well above the bulk transition [7, 8]. In bulk, another broad, subtle phase transition to a slightly orthorhombic structure occurs below roughly 65 K. There is furthermore some evidence of a transition below about 10 K to a third structural phase (possibly rhombohedral) [6].

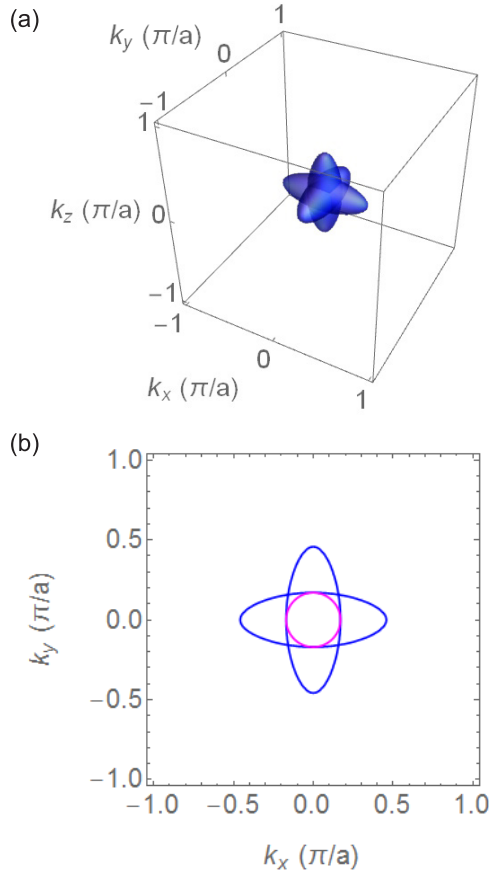


Figure 2. (a) Sketch of the bulk Fermi surface of STO at low doping in 3D. The ellipsoids oriented along the primary axes correspond to each of the t_{2g} bands. (b) Cut through the Fermi surface in the $k_x - k_y$ plane at $k_z = 0$.

The detailed structure and morphology of STO surfaces are generally quite sensitive to the conditions of the surface preparation. Structurally, the (001) surface, for example, can manifest a wide variety of reconstructions, depending on treatment conditions [9]. Surface diffraction experiments have also found evidence that TiO_2 -terminated STO can in certain cases become depleted of its first SrO underlayer, leading to a stable double- TiO_2 capping layer with a characteristic 2×1 surface ordering [10–12].

Yet despite the complications that can potentially arise, much of the appeal of using STO as a substrate for heterostructures such as LAO/STO actually stems from the relative ease with which high-quality, single-termination surfaces can be obtained. On the (001) surface, various acid etching procedures [13–15] or a more recently established ‘leaching’ process with deionized water [16] can be used to remove SrO from the surface. Subsequent annealing then leads to smooth, well-ordered terraces with unit-cell step height that are TiO_2 terminated. By combining such surface preparation with realtime deposition monitoring using reflection high-energy electron diffraction (RHEED), oxide films can be grown on STO with unit-cell precision.

1.2.2. Electronic structure and properties. Electronically, STO is an insulator with an indirect gap of about 3.25 eV between the predominantly O $2p$ valence and Ti $3d$ conduction

bands [17]. Electron doping is commonly achieved by substituting the cations with elements such as La or Nb, or by oxygen deficiency. Early calculations showed that doped electrons should occupy t_{2g} bands that, in the cubic phase, are degenerate at Γ and lie below the e_g manifold [18]. As depicted in figure 2, at low doping, each t_{2g} band corresponds to an ellipsoidal Fermi surface oriented lengthwise along one of the primary axes [19]. Thus the d_{xy} , d_{xz} , and d_{yz} ellipsoidal Fermi surface components are aligned along (001), (010), and (100), respectively. This band structure has been confirmed in ARPES experiments that managed to probe the bulk Fermi surface in heavily vacuum annealed conducting STO samples [20]. In low dimensional systems at interfaces and surfaces, the degeneracy of the occupied t_{2g} levels can be broken by symmetry and confinement. Strongly confined bands may form quantum well subbands [21] and/or be split by effects related to spin–orbit coupling (Rashba effect) [22]. These effects on the band structure in low-dimensional systems can be directly probed by ARPES and will be addressed in section 3.

While conducting oxide interfaces have garnered significant attention in recent years, there are still a number of open questions. In particular the origin of conducting electrons at the LAO/STO interface is still under debate. The so-called ‘polar catastrophe’ scenario, which gained early favor due especially to the observation that metallicity appears only when LAO exceeds a critical thickness of 4 unit cells [23], is based on the notion that electrons from LAO should transfer to STO in order to stabilize the polar discontinuity arising from the $(\text{LaO})^+ / (\text{AlO}_2)^-$ layer stacking in films grown on formally non-polar STO(001) [24]. Still, other factors such as oxygen vacancies or cation intermixing across the interface may play a role either in modifying the carrier density from the polarity-driven reconstruction, or perhaps bypassing the polar catastrophe mechanism altogether. Recently, in fact, the polar catastrophe scenario has been complicated by a number of striking discoveries, including quite similar conducting states formed in alternative systems such as LAO/STO(110), which formally lacks a polar discontinuity, and amorphous LAO grown over STO(001) [25]. Despite not fitting within the simplified polar catastrophe framework, these conducting interfaces, like the original LAO/STO(001), are nevertheless formed only after a certain critical thickness of the film has been deposited. Especially in light of the fact that nearly all known oxide conducting interfaces take place on STO, such results naturally raise questions about the polar catastrophe picture, and open the possibility that these interface electronic states arise from the unique properties of STO itself. The study of metallic surface states on bare STO and similar surfaces may shed some light on the origins of conductivity in TMO interfaces, since the role of a film overlayer can be excluded. Such issues will be discussed in section 5.

It must also be emphasized that bulk electron-doped STO is superconducting at low temperature with a maximal transition temperature close to $T_c = 300$ mK [26, 27]. Despite the seemingly low T_c , this behavior is actually quite astounding; Optimal doping occurs at an exceptionally low carrier density on the order of $n = 10^{20} \text{ cm}^{-3}$, which corresponds to only

about 6×10^{-3} electrons per unit cell. Within BCS theory, T_c has a roughly $\sim \exp[-1/n(E_F)]$ dependence on the density of states at E_F [28]. Thus, the superconductivity in STO suggests that anomalously strong pairing interactions may be present at low doping in order to compensate for the minuscule carrier density. LAO/STO interfaces can likewise become superconducting, with maximal T_c quite close to that of bulk STO [29]. Experiments have demonstrated gate-voltage control over the superconducting phase [30, 31], which is an exciting development for devices, as well as fundamental research into superconductivity.

1.2.3. Proximity to ferroelectricity. Another remarkable property of bulk STO, which could very well be related to its unusual superconductivity [32], is its so-called ‘incipient’ ferroelectricity. Other closely related titanates, PbTiO_3 and BaTiO_3 , are well known ferroelectrics with fairly high transition temperatures. STO, meanwhile, sits in proximity to a quantum critical phase transition to a ferroelectric state. Based on an observed saturation in the dielectric constant below 4 K, Müller and Burkard dubbed STO a ‘quantum paraelectric,’ meaning that ferroelectric phase fluctuations could be quantum mechanically stabilized at low temperature [33]. Notably, the compounds KTaO_3 and CaTiO_3 , which also host surface metallic states (section 3.6), show analogous quantum paraelectric behavior [34]. The quantum instability implies that even the smallest perturbation, e.g. to the A-site of the ABO_3 perovskite structure, might trigger a transition to true ferroelectricity. Indeed, Bednorz and Müller showed that $\text{Sr}_{1-x}\text{Ca}_x\text{TiO}_3$, even for a value as low as $x = 0.002$, acquired a peak in the dielectric constant at finite temperature characteristic of a ferroelectric phase transition [35]. Isotope-substituted $\text{SrTi}^{18}\text{O}_3$ is likewise found to be ferroelectric below about 23 K [36]. Moreover, STO thin films have been shown to be ferroelectric [37], and their transition temperatures can be tuned by via substrate-induced strain [38]. The ferroelectric tendency of STO and related d^0 perovskites is linked to distortion-enhanced covalency between the cation and O $2p$ states, coupled with softening of the corresponding optical phonon mode [39, 40]. Thus, like its superconducting behavior at low carrier density, STO’s incipient ferroelectricity is an indicator of the crucial role that phonon interactions may play in determining the electronic properties. Section 4 will present the spectroscopic signatures of polarons resulting from strong coupling of itinerant electrons to optical phonon modes in STO and related systems.

Related to the above, numerous experiments and calculations find that STO(001) surfaces exhibit static polar buckling distortions within the TiO_2 and SrO layers, which are not present in the bulk [41–44]. Surface Ti–O buckling, with O displacements above the Ti plane on the order of 0.1 Å, along with similar Ti–O buckling distortions observed at LAO/STO interfaces [45–47] is particularly suggestive that the quantum ferroelectric instability of bulk STO may tend toward static polarization at surfaces/interfaces, where translational symmetry is broken and/or particular defects may occur. As will be discussed in section 3, such distortions can have important

influences on the electronic and spin structures of the systems that will be presented.

1.2.4. Magnetism. Although nominally nonmagnetic, multiple groups have recently found evidence of magnetism in STO. Rice *et al* reported on magnetic circular dichroism and superconducting quantum interference device (SQUID) measurements of STO irradiated by sub-bandgap photons [48]. The authors found that persistent ferromagnetic states could be optically written into the material, and the direction of magnetization could even be controlled depending on the wavelength and polarization of the ‘pump’ photons. This behavior was only found in nominally oxygen-deficient STO. Rao *et al* reported similarly that STO could become ferromagnetic following laser irradiation, and related the phenomenon to oxygen vacancies, based on a strong reduction in the magnetic moment after annealing in oxygen [49].

The local versus itinerant nature of the magnetism is unclear. The results of Rice *et al* and Rao *et al* were argued to be due to local moments. However Liu *et al* found that Nb-doped STO is ferromagnetic without any irradiation and argued that the magnetism, though coupled to local moments from oxygen vacancies, was mediated by itinerant electrons [50]. There is furthermore emerging controversy as to whether the observed magnetism in STO is truly in the bulk [48, 49] or instead surface-related [49, 50].

Magnetism is also reported in LAO/STO interfaces [51], with evidence that ferromagnetic islands can even be found coexisting alongside the superconducting phase [52]. As in STO crystals, however, the precise explanation for magnetism at the interface and the nature of the magnetic order is unclear, and there are a number of theoretical proposals pertaining to various scenarios [53–56]. Experimental studies using x-ray magnetic circular dichroism (XMCD) have also arrived at conflicting conclusions [57, 58]. The situation is all the more complicated due to the fact that bulk and interface systems could have quite different magnetic properties due to dimensionality: spiral spin order, for example, has been proposed at the LAO/STO interface [54]. Spin-resolved ARPES showing evidence for magnetism on bare STO surfaces will be discussed in section 3.4.

2. Basics of angle- and spin-resolved photoemission

Here we offer a brief introduction to the relevant aspects of ARPES in the present context. For further reading, the theory and practice of the technique is covered in a number of textbooks and review articles [59–61].

ARPES makes use of the photoelectric effect in order to directly extract the energy- and momentum-resolved electronic structure of solids. An electrostatic analyzer measures the kinetic energies E_{kin} and emission angles α of electrons ejected by monochromatic photons with energy $h\nu$ (figure 3). This information can be mapped back to the electrons’ initial energies E_i and crystal momenta \mathbf{k} in the solid—i.e. the band structure. Taking into account the photon polarization with

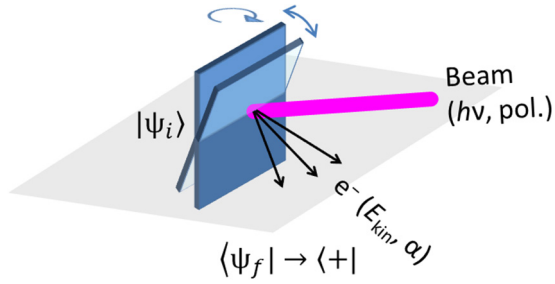


Figure 3. Simplified elements of ARPES. An incident photon beam with energy $h\nu$ and specified polarization impinges on the sample. Electrons are excited from initial states, $|\psi_i\rangle$ to final states $\langle\psi_f|$. The final state is a plane wave and thus has even parity (+) with respect to the scattering plane of the experiment (gray). The photoelectrons are analyzed in terms of their kinetic energies and emission angles, α .

respect to the experimental geometry, it is additionally possible to obtain information about the symmetries of the orbitals that compose the bands. Spin-resolved detectors can further quantify the spin polarization of the bands. Finally, ARPES data can be analyzed on even deeper levels to determine the influence of many-body interactions (e.g. electron–electron, electron-phonon, etc) on the dispersions and lifetimes of the electronic states.

Formally, the ARPES process corresponds to a quantum many-body propagator describing the single-particle removal function from the full Fermi sea. This full description is the so-called ‘one-step’ model. The problem is greatly simplified by invoking the sudden (i.e. non-adiabatic) approximation and breaking the process into three steps: a ‘Fermi golden rule’-type excitation, travel to the surface, and emission.

The photoexcitation step is expressed by the matrix element

$$M_{fi} = |\langle\psi_f|\mathbf{A} \cdot \mathbf{p}|\psi_i\rangle|^2 \quad (1)$$

describing the transition of the initial single-electron wavefunction ψ_i to final state ψ_f . The electromagnetic vector potential \mathbf{A} of the radiation depends of course on the polarization and the photon energy. Manipulating the sample geometry and/or polarization can thus be used to uncover transitions that are suppressed by symmetry, thereby providing information about the orbital compositions of the wave functions. Namely, $\langle\psi_f|$ is a plane wave with even parity with respect to the scattering plane of the experiment, leaving the parity of the product $(\mathbf{A} \cdot \mathbf{p})|\psi_i\rangle$ to be defined by the experimentalist (figure 3). In the present context, this technique has been used to verify the orbital characters of the conduction bands on oxide surfaces, in particular to distinguish the d_{xy} , d_{xz} , and d_{yz} orbitals of the t_{2g} manifold (see figures 4(a) and (b)). Nevertheless, matrix element effects can occasionally complicate the interpretation of ARPES spectra. In the first Brillouin zone of STO, for example, the bottoms of the bands are suppressed regardless of the photon polarization and cannot easily be discerned (figure 4(c)).

The emission step allows k -space mapping via the expression for the \mathbf{k} component in the surface plane, \mathbf{k}_{\parallel} , which follows directly from conservation of energy and momentum parallel to the sample surface:

$$\mathbf{k}_{\parallel} = (2mE_{\text{kin}}/\hbar^2)^{1/2} \sin \alpha. \quad (2)$$

Note that E_{kin} is referenced to the ‘vacuum level’ established by the material’s work function Φ :

$$E_{\text{kin}} = E_i - E_F + h\nu - \Phi. \quad (3)$$

Momentum perpendicular to the surface, k_{\perp} (often also called k_z), is not conserved due to the work function. However, when the final states of the photoexcitation process are taken to be free-electron-like (a reasonable approximation for sufficiently large $h\nu$), the quantity can be written as

$$k_{\perp} = [2m(E_{\text{kin}} \cos^2 \alpha + V_0)/\hbar^2]^{1/2}, \quad (4)$$

where V_0 is a constant called the ‘inner potential’. Evaluating this equation at fixed E_{kin} , we see that a given photon energy accesses a sheet of k_{\perp} values that is curved as a function of emission angle (i.e. as a function of k_{\parallel}). In practice, one probes k_{\perp} by observing the periodic dependence of the band structure on $h\nu$, which allows V_0 to be determined. From equations (2) and (4), a scan of the emission angles at a given $h\nu$ thus maps the photoelectron intensity at \mathbf{k}_{\parallel} points projected on a slightly curved sheet of k_{\perp} values. Thus, broadly tunable vacuum ultraviolet and x-ray photon sources (namely synchrotron beamlines) are invaluable for performing ARPES in 3D electronic systems. This turns out to be surprisingly relevant for understanding the electronic structure of metallic systems at oxide interfaces. As we will discuss in section 3.3, recent ARPES results have shown how the conducting electron states on, e.g. the STO surface penetrate toward the bulk and display orbital-dependent quasi-3D character.

With these relations in hand, one then measures the intensity

$$I(\mathbf{k}, E) = A(\mathbf{k}, E) M_{fi} f(E, T) \quad (5)$$

equal to the spectral function $A(\mathbf{k}, E)$, multiplied by the Fermi–Dirac distribution $f(E, T)$ and photoexcitation matrix elements M_{fi} . The crucial point here is that $A(\mathbf{k}, E)$ is not merely the non-interacting, ‘bare’ band structure, $\epsilon(\mathbf{k})$. Rather, it is $\epsilon(\mathbf{k})$ modified by many-body interactions of the system (electron–electron, electron-phonon, etc). In the field theoretic description, these interactions are encoded in the complex self-energy, $\Sigma(\mathbf{k}, E) = \Sigma'(\mathbf{k}, E) + i\Sigma''(\mathbf{k}, E)$ within the single-particle removal Green’s function, and the spectral function can be obtained as

$$A(\mathbf{k}, E) = \frac{1}{\pi} \frac{\Sigma''(\mathbf{k}, E)}{[E - \epsilon(\mathbf{k}) - \Sigma'(\mathbf{k}, E)]^2 + [\Sigma''(\mathbf{k}, E)]^2}. \quad (6)$$

We can therefore clarify the role of interactions in ARPES spectra: when interactions are minimized (i.e. $\Sigma \rightarrow 0$), the peaks of the spectral function will simply be the bare band structure $\epsilon(\mathbf{k})$. But turning interactions on shifts the bands according to $\Sigma'(\mathbf{k}, E)$ and broadens them according to $\Sigma''(\mathbf{k}, E)$. Depending on their strengths, energies, and momenta, interactions can lead to dramatic features such as dispersion ‘kinks’ or spectral redistribution in the form of humps or energy-shifted replica bands, which can be analyzed in order to extract information about the interactions coupling to the electrons.

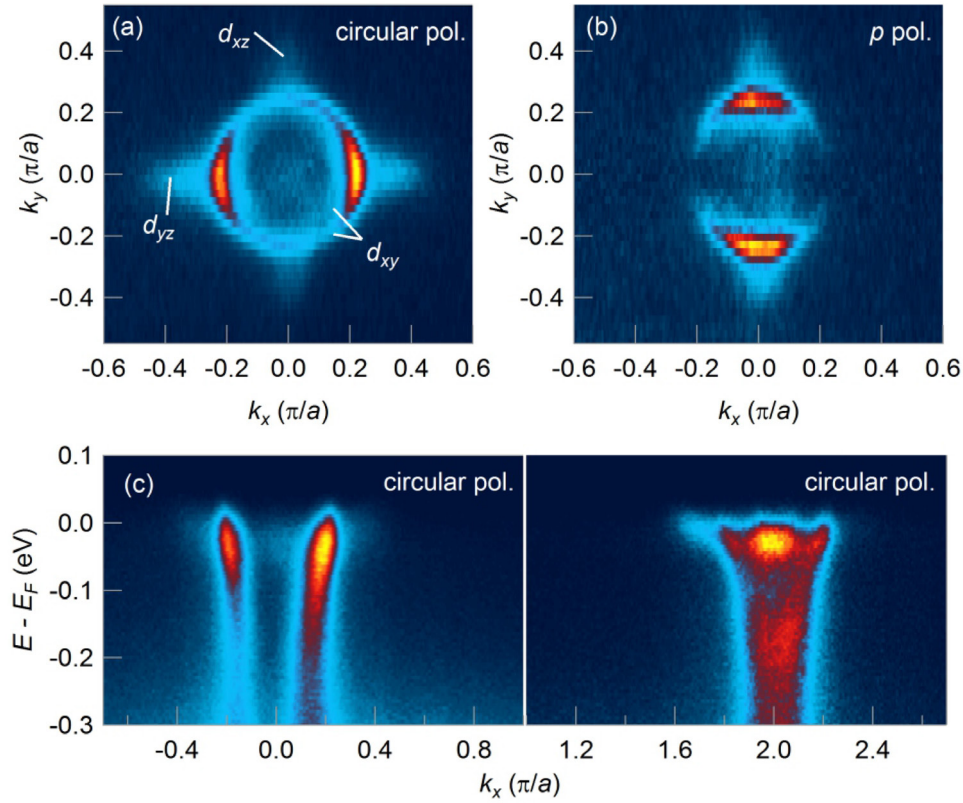


Figure 4. Matrix element effects in STO. (a) Fermi surface of the STO(001) surface state obtained using 85 eV circular polarized photons. (b) The same scan performed with p -polarization. Under the experimental geometry, dipole selection rules suppress the photoemission signal from the d_{xy} and d_{yz} bands when the sample is tilted normal to the scattering plane (which occurs at $k_y = 0$). (c) Dispersion viewed along k_x at $k_y = 0$. It is found that matrix element effects strongly reduce the signal at $k_x = 0$, leading to ‘waterfall’-shaped dispersions. By contrast, the proper band bottom can be seen in the zone centered at $k_x = 2\pi/a$. The data were obtained with 85 eV circular polarized photons.

The use of detectors based on preferential spin scattering (e.g. Mott scattering) enables spin-resolved ARPES (SARPES) [62]. Two detectors can be used in combination to determine the spin polarization vector in 3D. Although spin resolution brings obvious advantages and despite the well-established success of the technique, SARPES is an experimentally demanding probe. The detectors are single- or few-channel, rather than 2D as in spin-integrated ARPES, and the energy and momentum resolution typically suffer in order to compensate for the drastically reduced count rates due to inefficiency in the spin-scattering process of the detector. In addition, SARPES measurements can be complicated by matrix element effects, which in dramatic cases can even lead to measured spin polarization *opposite* to that of the initial state [63–65]. These effects can arise due to spin–orbit interaction, since the entanglement of the spin and orbital angular momenta means that the *observed* spin can be influenced by orbital matrix element effects. The measurements may also be affected by interference between the wavefunctions of the outgoing photoelectrons. As will be discussed in section 3.4, the spin structure of the STO(001) surface is currently under dispute, and such experimental complications might be contributing to the disagreements.

Finally, in any discussion of photoemission techniques, it is important to take into account the inherent surface sensitivity due to the electron inelastic mean free path, which, for

typical ARPES photon energies in the vacuum ultraviolet, is generally under 1 nm [66]. The electron escape depth can be improved somewhat by moving either to lower or higher energies (UV lasers or soft/hard x-rays, respectively). However, obtaining ARPES data from the buried LAO/STO interface has proven exceptionally demanding, and it has been necessary to greatly enhance the signal by performing measurements at photon energies resonant with Ti L absorption. These experiments will be discussed in section 3.5.

Due to the extremely short escape depths of photoelectrons, preparing clean, flat surfaces is critical to obtaining good ARPES data. In many materials, excellent surfaces can be obtained by a straightforward cleaving procedure in ultrahigh vacuum (UHV). This unfortunately is not the case for cubic perovskites such as STO, which lack a natural cleavage plane. In most cases, for the materials addressed here, ARPES was performed on surfaces that were scraped or fractured in UHV, which is obviously a quite uncontrolled process. However, some studies have used alternative approaches, such as chemical etching followed by *in situ* annealing, *in situ* ion sputtering and annealing, fracturing followed by *in situ* oxygen surface dosing, or even fully *in situ* growth of LAO/STO interfaces in the measurement system. These preparations can have positive effects on data quality and in some limited cases lead to noticeably modified features [67, 68].

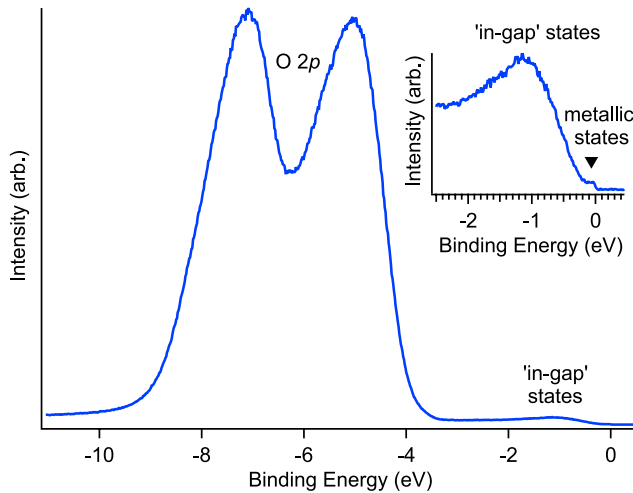


Figure 5. Representative momentum-integrated photoemission spectrum acquired from STO(001) showing the O 2p valence band, in-gap states, and metallic states at the Fermi level. The inset highlights the near- E_F region.

3. Electronic structure of STO(001) and related systems

3.1. Early photoemission experiments on STO

Interest in the surface electronic structure of STO dates back to at least the 1970s and was prompted in large part by the catalytic properties of titanates [69, 70]. Theoretical studies by Wolfram and coworkers based on the linear combination of atomic orbitals (LCAO) method indicated that d band surface states inside the bulk band gap could be intrinsic features of STO and similar materials such as TiO_2 and KTaO_3 [71–73]. A number of angle-integrated photoemission spectroscopy (PES) experiments performed on fractured STO surfaces observed a weak signal inside the bandgap consisting of a peak centered at roughly 1 eV binding energy with its tail extending quite close to (or possibly up to) E_F . This was identified as a surface feature and proposed to be defect-related, since it was found to be enhanced by treatments such as Ar^+ sputtering [74], as well as annealing in either vacuum or oxygen [75], and its signal disappeared upon exposing the surface to oxygen [74]. Later Aiura *et al* found a sharp feature at E_F in addition to the broader in-gap signal previously seen at roughly 1 eV binding energy. This energetic landscape is illustrated in figure 5. Like the deeper in-gap states, the feature at E_F vanished after dosing the surface with a very low amount of oxygen (< 0.3 Langmuirs), confirming that it too was surface-related [19].

3.2. Uncovering the metallic surface state on STO(001)

The first ARPES spectra showing a surface state on STO was obtained by Meevasana *et al* in 2010 [76]. There the authors were attempting to look at bulk band features in lightly-doped $\text{La}_x\text{Sr}_{1-x}\text{TiO}_{3+\delta}$ samples prepared by cleaving on the (001) surface. Spectra acquired in the photon energy range of $h\nu = 19 - 29$ eV showed shallow bands centered at Γ dispersing down to ~ 50 – 60 meV below E_F , whose appearance and k_F momenta were sensitive to the photon energy and thus

consistent with bulk (or bulk-like) bands. Another deeper dispersing band, however, did not change with photon energy, leading the authors to conclude it was a surface state.

Two ARPES studies quickly followed in the next year and drew significant attention to the surface electronic structure. Santander-Syro *et al* studied cleaved (001) surfaces of nominally undoped STO samples, as well as samples with varying levels of electron doping due to bulk oxygen vacancies generated by vacuum annealing. Using photon energies of 45 and 47 eV, multiple bands could be seen in ARPES E -versus- k cuts: a set of bands with low effective mass and at least one shallower ‘heavy’ band as seen from cuts along the (100) direction [77]. Astoundingly, the observed bands’ k_F momenta (and hence the corresponding Fermi surface size and carrier density) were found to be essentially identical, regardless of the bulk doping of the samples—even on nominally undoped samples. This behavior was portrayed in dramatic fashion by showing the similarities between ARPES spectra from wafers whose appearances in photographs ranged from transparent to black. The authors reasoned that the ‘universal’ bands must be surface states associated with a downward band bending, speculated to be due to oxygen vacancies generated in the process of cleaving the surfaces.

Nearly at the same time, Meevasana *et al* published an investigation of cleaved 0.1% La-doped STO(001) samples using photon energies in the range of 45–60 eV, focusing especially on $h\nu = 55$ eV [78]. At these photon energies, the surface state features could be isolated, revealing at least two bands forming circular Fermi surfaces at the Γ point, consistent with the bands having $\text{Ti } 3d_{xy}$ character and similar to two light bands seen by Santander-Syro *et al*. The authors also observed that the bands were being formed during irradiation of the sample in the synchrotron beam. As in the work of Santander-Syro *et al*, oxygen vacancies—this time thought to be photoinduced—were suspected to be responsible for downward band bending in the surface region. In support of this picture, the authors noted a decrease in spectral weight from the O 2p valence band, concomitant with an increase in photoemission intensity from the in-gap states centered near -1.3 eV binding energy.

In broad strokes, the findings from these two studies were similar: under certain experimental conditions, STO can exhibit a surface state on the (001) surface, with a pair of low-effective-mass electron-like bands dispersing down to roughly 200 and 100 meV below E_F . Estimates of the 2D carrier density from these measurements were also in rough agreement, ranging from $8 \times 10^{13} \text{ cm}^{-2}$ to $2 \times 10^{14} \text{ cm}^{-2}$ (0.1–0.3 electrons per planar unit cell). However, there were some apparent contradictions as well. Santander-Syro *et al* had observed more bands than Meevasana *et al*, and the two studies offered different proposals regarding the orbital character of the 100 meV band. Moreover, although both groups suspected that band bending responsible for the surface state was due to surface oxygen vacancies, the evidence for this was somewhat hard to reconcile. On one hand, the surface state was astoundingly robust to oxygen vacancies from vacuum annealing, but on the other hand, it was acutely sensitive to photon irradiation. Adding to this complicated story,

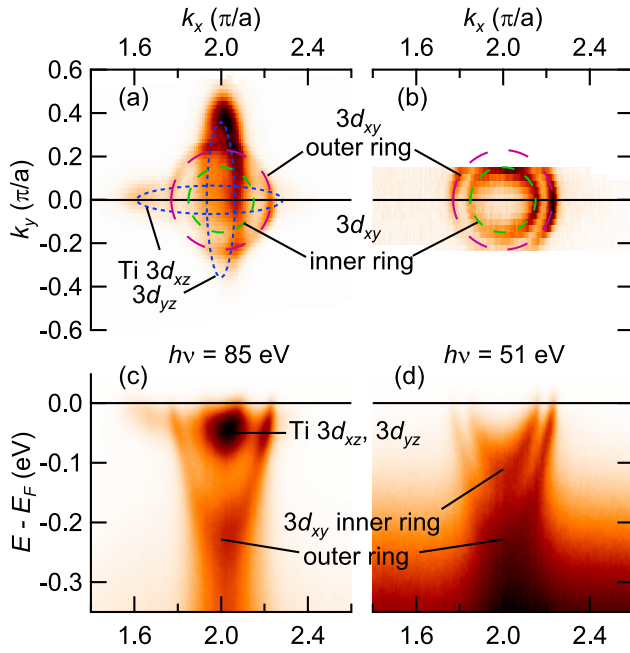


Figure 6. Conduction band structure of STO(001). (a) and (b) Fermi surfaces in the surface $k_x - k_y$ plane acquired using $h\nu = 85$ and 51 eV, respectively. (c) and (d) Dispersion along k_x evaluated at $k_y = 0$ for each photon energy. The ring-shaped d_{xy} and elliptical d_{xz}/d_{yz} Fermi surface components are indicated. Adapted with permission from [80]. Copyright (2014) by the American Physical Society.

scanning tunneling spectroscopy experiments found evidence for a surface state on STO(001) samples annealed in UHV at 250°C and 350°C , but generating relatively high levels of oxygen vacancies by annealing at 900°C opened an insulating gap [79]. Similarly annealed STO samples studied by ARPES exhibited only (small) bulk-like Fermi surfaces, rather than surface states [20].

3.3. Clarifying the bands and their orbital-dependent dimensionalities

Subsequent work by Plumb *et al* addressed questions regarding the various bands comprising the STO(001) surface state and showed that the previous studies' observations were complimentary, rather than contradictory [80]. Detailed spectra obtained in fine increments of the photon energy from $h\nu = 35$ eV to 95 eV (corresponding to more than one full Brillouin zone along k_z) consistently showed the presence of the circular Fermi surface components with d_{xy} character. In addition, shallower bands forming a pair of crossing ellipsoidal Fermi surface components, consistent with d_{xz}/d_{yz} orbital character, could be observed at select photon energies. Examples obtained with photon energies of 85 eV and 51 eV are shown in figure 6. Based on the detailed photon energy dependence, the d_{xy} bands were clearly demonstrated to be highly 2D, while the d_{xz}/d_{yz} were argued to be (quasi-)3D. Yet surprisingly, when viewed in 3D momentum space, the d_{xz}/d_{yz} Fermi surface ellipsoids seemed to be shaped more like discs or 'flying saucers' than like 'cigars,' as expected in bulk symmetry, suggesting these states had an enhanced effective mass along the surface normal (001) axis (figure 7). In other words,

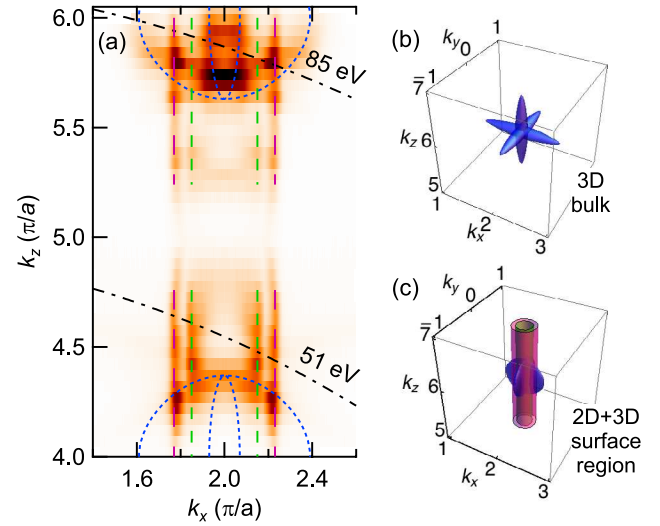


Figure 7. (a) Fermi surface of STO(001) in the surface-perpendicular $k_x - k_z$ plane, evaluated at $k_y = 0$. Black dashed-dotted lines indicate the locations in k_z of the $k_x - k_y$ maps obtained using 85 and 51 eV photons in figures 6(a) and (b), respectively. (b) Depiction of the expected Fermi surface of bulk STO in contrast to (c) a schematic rendering of the observed surface state with a mixture of quasi-2D and -3D components. Adapted with permission from [80]. Copyright (2014) by the American Physical Society.

the observed d_{xz}/d_{yz} bands showed spectroscopic signatures of being quasi-3D, *non-bulklike* electron states associated with some finite near-surface region.

The confinement of the metallic d_{xz}/d_{yz} states to the near-surface region was confirmed by examining the Fermi surface as a function of bulk doping. Working from etched, predominantly TiO_2 -terminated samples, rather than uncontrolled, cleaved ones, the authors acquired Fermi surface maps using $h\nu = 85$ eV, which allowed the simultaneous observation of both the d_{xy} and d_{xz}/d_{yz} components. Not only the d_{xy} bands previously highlighted by Santander-Syro *et al*, but also the d_{xz}/d_{yz} Fermi surface components were found to be 'universal' in size and shape with respect to a broad range of dopings and *in situ* treatments, ranging from annealing at 550°C in 100 mbar of O_2 (nominally undoped; bulk insulating and optically transparent) to 720°C in UHV (bulk conducting and opaque black) to niobium-doped STO (also bulk conducting and opaque black).

The exact spatial extent of the d_{xz}/d_{yz} states from the surface toward the bulk cannot be determined directly from ARPES, but is presumably a few to some dozens of unit cells, judging from tight-binding simulations [81], as well as calculations predicting a qualitatively similar finite region of carrier confinement in LAO/STO [21, 82]. At this lengthscale, discrete, finely-spaced quantum well states (with larger spatial extent for higher quantum number n) would ostensibly merge and take on a certain periodic photon energy dependence, leading to the appearance of the k_z dispersion seen in ARPES. The layer-by-layer evolution of ARPES spectra from multilayer graphene can be considered illustrative of this crossover [83].

As sketched qualitatively in figure 8, the orbital-specific dimensionalities of the carriers in the STO(001) surface state

leads to a rather unique spatial-orbital arrangement of the conduction electrons in the near-surface region. Away from the surface, carriers solely occupy bands with d_{xz}/d_{yz} character while the d_{xy} states lie above the Fermi energy. At the surface, however, both types of orbitals are partially occupied, but their energetic order is reversed, with d_{xy} bands descending below the d_{xz}/d_{yz} states. King *et al* independently arrived at a similar conclusion regarding the spatio-orbital order based on comparing a tight-binding model with ARPES data [81]. Results from other experiments and calculations suggest that the orbital-dependent dimensionality and the transition from a d_{xy} -dominated, multiorbital Fermi surface to a purely d_{xz}/d_{yz} -based Fermi surface with increasing distance from the interface is a quite common feature in the context of STO(001), regardless whether the interface in question is formed with vacuum or, e.g. LAO [21, 84, 85] or the Mott insulator LaTiO_3 [86].

The robustness of this electronic structure with respect to sample preparation and bulk doping/defects was observed alongside the photo-induced behavior reported by Meevasana *et al*, in which a substantial decrease in intensity from the O 2p valence band occurred alongside an increase in the in-gap states at roughly 1 eV binding energy. However, simultaneous measurements of the O 1s core level over the course of irradiation painted a more complicated picture of the formation of the surface state than might naively be assumed. Moreover, subsequent studies have demonstrated the Fermi surface ‘universality’ is not quite as robust as initially portrayed; there are in fact ways to tune the surface carrier density on STO surfaces, although the maximum consistently appears to be near the upper limit observed in early papers on the subject [68, 87]. These and other issues will be discussed in detail in section 5.

3.4. Spin-resolved electronic structure of STO(001)

The spin structure of the STO(001) surface state has been a matter of significant controversy in the field. On general grounds, a spin-splitting should exist in the system due to the Rashba effect; the debate is over the size of the splitting, and whether or not magnetism is present. The correct answer is of fundamental importance for understanding the nature of the observed bands, as well as how magnetism might arise in a surface or interface state of an otherwise non-magnetic oxide. It also carries significant practical importance, since large spin splitting on STO’s surface would set sights on new performance targets for oxide spintronic devices.

Whenever a surface or interface introduces an inversion symmetry-breaking potential in a crystal, spin-orbit coupling will result in so-called Rashba(-like) splitting [88, 89], which breaks the spin degeneracy of states with non-zero \mathbf{k} , with the spin orientations of the split bands locked tangentially to the electron momenta in counter-winding patterns (figure 9(a)). The simplistic explanation for this effect is that, via Lorentz transformation, electrons moving relativistically in the non-inversion-symmetric potential experience an effective magnetic field that breaks the spin degeneracy. There are two crucial things to note here: (1) In real systems, the true Rashba

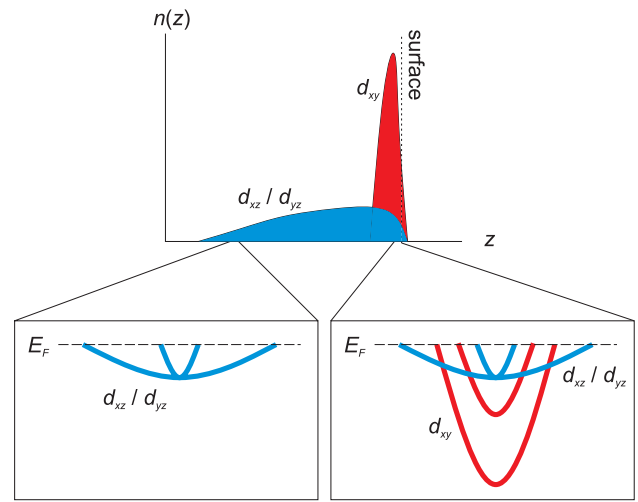


Figure 8. Qualitative sketch of the depth-dependent carrier density, $n(z)$, and spatial arrangement of occupied orbitals in the near-surface region of STO(001), as inferred from ARPES. The quasi-2D and non-bulklike 3D characters of the d_{xy} and d_{xz}/d_{yz} bands, respectively, signal that the energetic hierarchy of these states inverts as a function of distance from the surface, z .

effect is often orders of magnitude larger than theoretical estimates from simplified models. This reflects that the asymmetry of the wavefunction needs to be accurately accounted for at the atomic level. In principle, density functional theory is well-suited to this task, but the calculations must be based on the correct structure. (2) By itself, Rashba splitting leaves the spin states degenerate at the Γ point, and this so-called Kramers degeneracy can only be lifted by breaking time-reversal symmetry.

The first spin-resolved ARPES study of the STO(001) surface state indicated that the lowest two d_{xy} bands had opposite-winding spin polarizations, consistent with a Rashba-like splitting pattern [90]. In addition, the non-degeneracy of these bands at Γ implied that time reversal symmetry must be broken by a magnetic state. In further support of this picture, the electrons near E_F were measured to be fully spin-polarized in-plane, with decreasing length of the total spin polarization vector at energies and momenta near the Γ point. As the authors showed in supplementary information, this structure is consistent with a Rashba-dominated spin-splitting, plus an additional Zeeman splitting component near $k = 0$, whose contribution to the measured spin polarization would average to zero due to magnetic domains. These findings were somewhat surprising. Until then these bands, which are separated by roughly 100 meV, had been understood as distinct quantum well states. Moreover, an estimate of the Rashba parameter on the basis of the surface band bending predicts almost an order-of-magnitude lower value of the splitting [90], and previous tight-binding modeling had suggested that the splitting should be small (likely below the measurement limit) [81]. The Rashba-like splitting reported on STO(001) is also substantially larger than reported in LAO/STO interfaces based on magnetotransport measurements [22].

On the other hand, the same magnetotransport study revealed that Rashba-like splitting in LAO/STO shows a strong dependence on applied gate voltage. Thus, the splitting

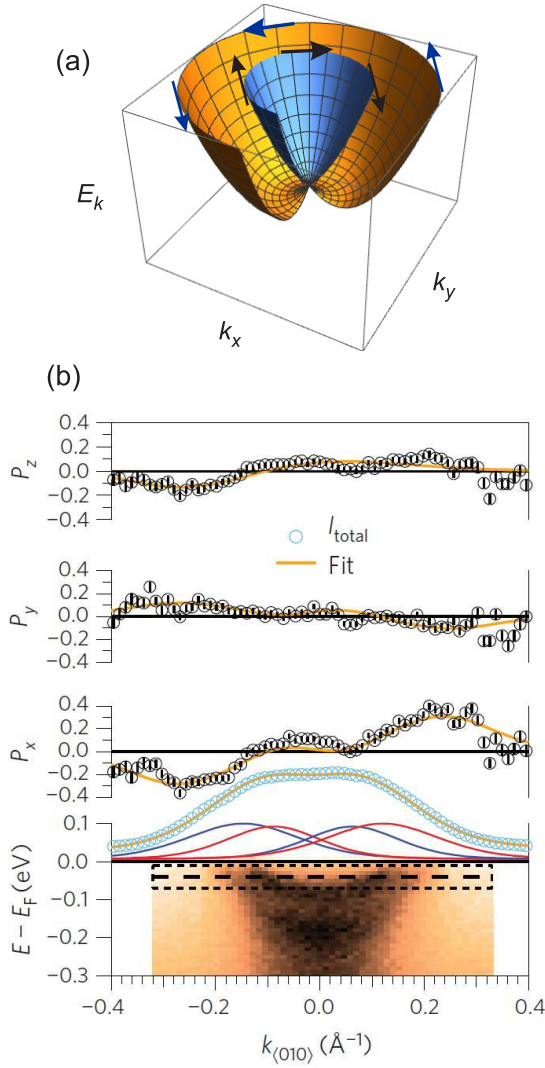


Figure 9. (a) Schematic of simple Rashba-like splitting. The electrons are spin polarized tangential to inner and outer bands and in opposite directions (arrows). The dispersions are degenerate at Γ , obeying time-reversal symmetry. (b) Subset of SARPES measurements on STO(001) reported in [90]. The upper curves show the components of the spin polarization P_x , P_y , and P_z measured along k_y , with $k_x = 2\pi/a$. In this configuration, x is out of the page, tangential to Fermi surface, and the shape of P_x , as well as the relatively flat P_y and P_z , are typical of the signal given bands exhibiting Rashba-like spin splitting. The bottom panel shows the band dispersion, with the dotted region indicating the integration window of the spin detector. The appearance of a gap at Γ implies that time-reversal symmetry is broken by magnetic order. Panel (b) adapted from [90] with permission.

on the surface should be quite sensitive to the details of the band bending, doping, and surface structure (e.g. ferroelectric-type distortions). Indeed ‘giant’ Rashba splitting is found to arise in systems where seemingly minor surface distortions enhance the local electric field and asymmetry of the electron wavefunction at the atomic scale [91, 92], which could certainly be applicable to STO(001), given the surface Ti-O buckling discussed in section 1.2.3. Meanwhile the magnetism in the STO surface state implied by the results of Santander-Syro *et al* is perhaps not so surprising at this point, given other recent observations in STO [48–50, 93] and LAO/STO [51, 52, 94, 95]. Unfortunately, the observation of broken

spin degeneracy at Γ is not able to reveal whether the inferred magnetism is local or itinerant in nature, nor whether it is ferromagnetic or of some other order (e.g. spiral), nor whether it is intrinsic or defect-related. None of these possibilities can be ruled out yet, and theoretical studies concerning LAO/STO have presented many potential scenarios for magnetism in these regards [5, 53, 54, 56, 96].

A more recent SARPES investigation reported no evidence for giant spin splitting in the STO(001) surface state [97]. The lack of an observable spin polarization in those experiments is argued to be consistent with the original quantum well interpretation of the d_{xy} subbands, each of which would presumably have Rashba-like spin-splitting below the measurement threshold [81]. Follow-up studies will be necessary to identify the reason for the discrepancy, since the experimental methods differed in potentially important ways. The measurements in the later work by McKeown Walker *et al* were obtained with $h\nu = 80$ eV in s -, p -, and circular polarization modes, as well as with 100 eV s -polarized photons. Meanwhile, in the initial study by Santander-Syro *et al*, the authors had verified the measurements of a Rashba-like spin texture at photon energies of 47 eV and 52 eV, each with s -, p -, and circular-polarization modes. The various photon energy regimes access different parts of the Brillouin zone in 3D, altering the relative contributions from the quasi-2D d_{xy} and -3D d_{xz}/d_{yz} bands to the total intensity. For example, the d_{xz}/d_{yz} bands, which one would not expect to show significant Rashba-like splitting on account of their dimensionality, tend to contribute much more to the total measured signal at 80 eV than at 47 eV, where the quasi-2D d_{xy} bands dominate. Furthermore, possible matrix element and/or photoelectron interference effects may be significantly different between the two sets of experiments.

We note that the two experiments also differed in terms of their scanning methods. Santander-Syro *et al* collected so-called momentum distribution curves of the full 3D spin-polarization vector at various fixed binding energies. By contrast, McKeown Walker *et al* measured energy distribution curves of the spin polarization along two component axes at two fixed k points. These distinctions might be crucial. The former approach has the advantage of surely sampling points from the relevant band structure but the disadvantage of changing the experimental geometry while doing so, thereby complicating any possible matrix element or interference effects. The latter approach, on the other hand, allows the measurements to be performed with fixed geometry, but the results could be rather sensitive to the positioning of the evaluated k points.

Other aspects of the experiments seem less likely to give a satisfying explanation for the differing results. The experimental resolutions were roughly comparable. Moreover, the sensitivity of spin-resolved ARPES is usually not severely hampered by resolution effects; the spin polarization signal is obtained from taking the difference between spin up and down channels, which frequently allows features to be detected that are finely spaced in comparison to the resolution. Differences in sample preparation methods also seem unlikely to play a role, given the robustness of the overall band structure demonstrated in previous work.

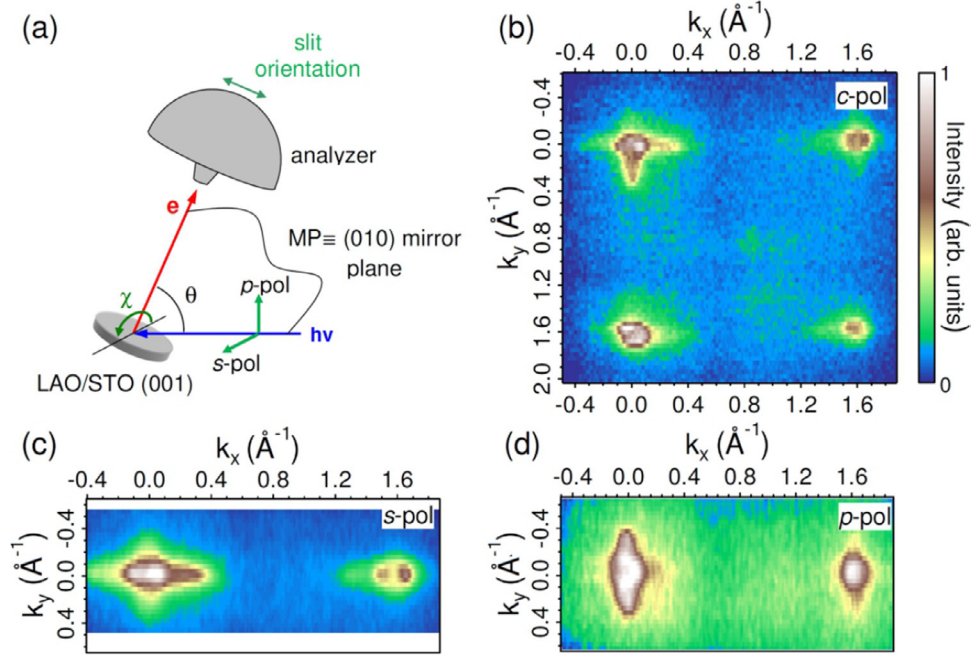


Figure 10. Fermi surface map of an LAO/STO interface acquired by performing resonant ARPES at the Ti L -edge. (a) Depiction of the experimental geometry. (b) Fermi surface measured using circularly polarized photons. (c) and (d) Maps acquired using s - and p -polarized photons, respectively. Reprinted figure with permission from [99]. Copyright (2014) by the American Physical Society.

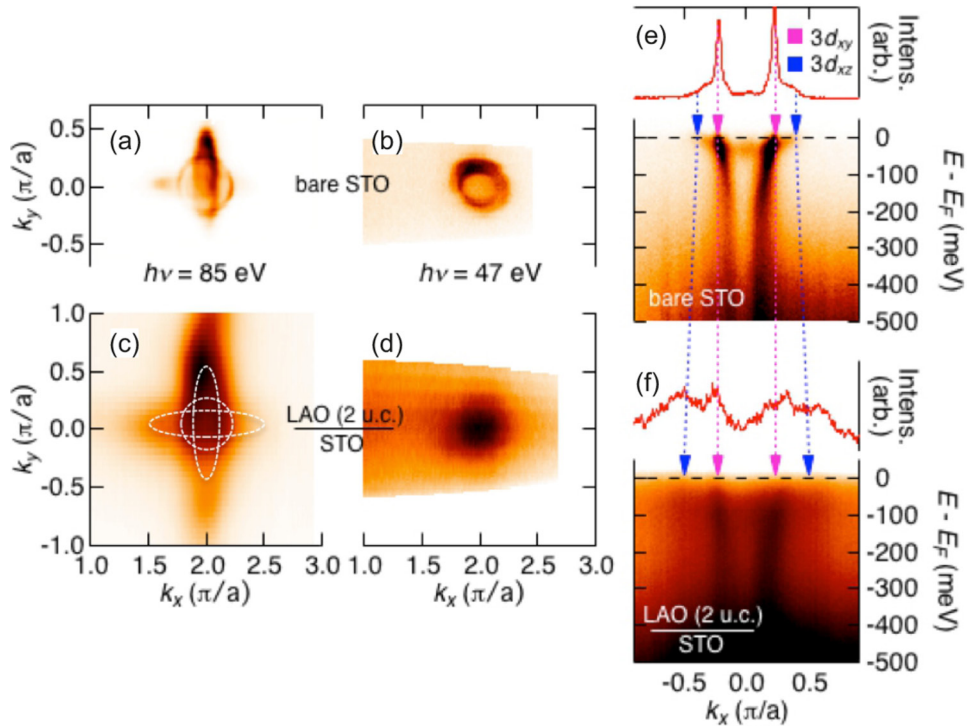


Figure 11. Comparison of ARPES from bare STO(001) and 2 uc LAO/STO. Fermi surfaces are formed in both systems following irradiation with the synchrotron beam. (a) and (b) Fermi surface maps from STO(001) acquired using $h\nu = 85$ eV and 47 eV, respectively. (c) and (d) Analogous maps from 2 uc LAO/STO. The Fermi surface sketched by the dashed white lines in (c) is based on the main features observed at 85 eV in (a). The photon energy dependence illustrates that 2 uc LAO/STO has a similar mixture of orbital-dependent quasi-2D and -3D carriers (see section 3.3). (e) and (f) Comparison of dispersion cuts along k_x evaluated at $k_y = 0$. Reprinted from [85], with permission from Elsevier.

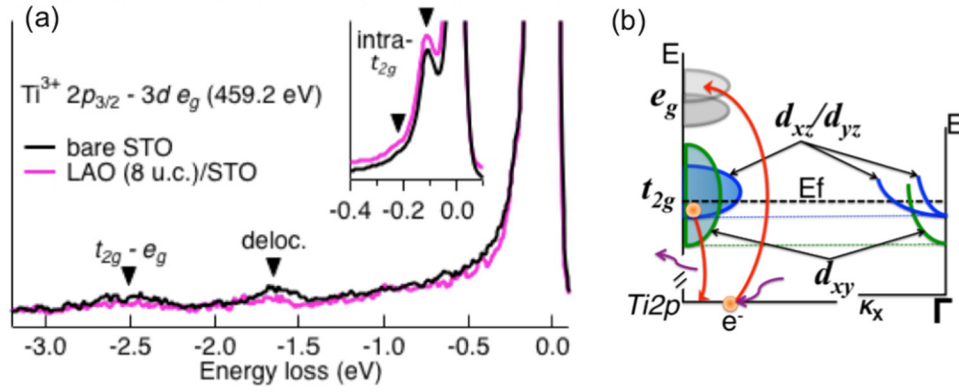


Figure 12. (a) Comparison of Ti^{3+} L -edge RIXS spectra from bare STO and LAO/STO. Similar dd excitation features are seen ($t_{2g} - e_g$ and intra- t_{2g}), indicating that the crystal fields are non-cubic and nearly identical. (b) Schematic of the d orbital splitting. Adapted from [85], with permission from Elsevier.

3.5. LAO/STO

In order to view the momentum-resolved band structure of LAO/STO interfaces, recent studies have succeeded in overcoming ARPES's shallow probing depth by using resonant photon energies at the Ti $L_{2,3}$ -edge (roughly 458–465 eV), which strongly enhance the photoemission signal from the Ti-derived conduction bands. Berner *et al* demonstrated that the Fermi surface in LAO/STO(001) exhibits crossed ellipses, consistent with theoretical expectations [98]. The authors moreover identified non-dispersive in-gap states at roughly 1–2 eV binding energy. From investigating the Fermi surface (figure 10) using alternately s - and p -polarized photons, Cancellieri *et al* were able to experimentally verify the d_{xz}/d_{yz} band character of the elliptical Fermi surface components, and dispersion cuts showed evidence of one d_{xy} band, which is more dispersive than the d_{xz}/d_{yz} bands [99]. The Fermi surface volumes in both studies appear similar, corresponding very roughly to a few times 10^{13} cm^{-2} (though notably, Cancellieri *et al* reported that the value can be tuned slightly by the LAO growth temperature). This value is in line with transport data from LAO/STO interfaces [23] but also below the expectation of half an electron per unit cell (10^{15} cm^{-2}) in the pure polar catastrophe model. It is also in the same realm as the carrier density on bare STO(001). Thus, in terms of its Fermi surface, in-gap states, and carrier density, the band structure of the LAO/STO interface closely resembles the STO surface. Moreover, as will be discussed further in section 4, both systems show signatures of strong electron-phonon coupling in the form of polarons.

These observed similarities between bare STO and LAO/STO interfaces prompted a combined spectroscopic study using both conventional high-resolution and resonant ARPES, as well as resonant inelastic x-ray scattering (RIXS) [100], to investigate STO(001) as a function of LAO deposition thickness [85]. The authors discovered that, similar to bare STO, a conducting state could form due to irradiation on STO covered by only two unit cells (uc) of LAO (i.e. below the standard critical thickness for interface conductivity). Thanks to the low film thickness, high-resolution ARPES data could be obtained and was found to be quite similar to bare STO in

terms of split d_{xy} and d_{xz}/d_{yz} bands and their mixed quasi-2D and -3D characters, respectively, with the Fermi surface being only slightly larger in the 2 uc LAO/STO sample (figure 11). The profound similarity of the bare STO and LAO/STO systems was affirmed by RIXS performed at the L -edge of Ti^{3+} species associated with the metallic state. As shown in figure 12, energy loss features corresponding to intra- d -band excitations exhibited nearly identical crystal fields for Ti^{3+} in STO and 8 uc LAO/STO (i.e. well above standard critical thickness). A previous RIXS study on LAO/STO multilayer heterostructures had identified the same splitting pattern as resulting from non-cubic symmetry [101]. Interestingly, however, resonant ARPES found a Fermi surface folding (likely of 2×1 order) in samples with four or more unit cells of LAO, indicating the presence of an in-plane structural reconstruction at the interface. While the reconstruction had not been identified in earlier resonant ARPES studies and could be defect-related, the authors noted that annealing in oxygen did not alleviate the folding and proposed the possible existence of defect- and/or strain-induced tilting of the TiO_6 octahedra. The in-plane reconstruction thus highlights one way in which interfacial conducting systems may differ from bare oxide surfaces, despite being intimately connected in terms of overall band structure, which in turn could lead to important new routes for engineering and experiments.

3.6. Other surface orientations and materials

A number of recent studies have revealed conducting surface states formed on various surfaces of STO, as well as on closely related materials (all d^0 oxides with octahedrally coordinated cations). ARPES measurements of the STO(110) and STO(111) surfaces demonstrated how the Fermi surface can be tuned by the surface orientation, leading, for example, to a set of fully degenerate bands confined on STO(111) [102–104].

Other ARPES investigations reported surface states formed on $\text{KTaO}_3(001)$ [105] and (111) [106]. KTaO_3 shares a number of properties with STO, including quantum paraelectric behavior (section 1.2.3), although spin-orbit coupling

effects should be stronger in KTaO_3 due to tantalum's higher mass. Indeed, $\text{KTaO}_3(001)$ was found to exhibit an especially interesting electronic structure with a sequence of strongly split d_{xy} , d_{xz} , and d_{yz} subbands showing evidence of strong spin–orbit coupling. Even more recently, a highly 2D state has been observed on the (001) surface of thin films of another quantum paraelectric material, CaTiO_3 [107]. In the case of CaTiO_3 , the Fermi surface consists of only a single d_{xy} band, indicating that the splitting between the t_{2g} states is larger than the occupied bandwidth (i.e. greater than about 400 meV). The system also undergoes a particularly interesting response to photon irradiation, changing from an initial $c(4 \times 2)$ to a $p(2 \times 1)$ surface reconstruction under illumination, while the photoemission signal from the metallic state intensifies.

Surface states have also been found to form on the (001) and (101) surfaces of anatase TiO_2 [108]. Both surface states consisted of a pair of d_{xy} subbands. In the (001) orientation, the subbands formed rings that appear quite similar to the d_{xy} bands on $\text{STO}(001)$, while moving to the (101) orientation led to an anisotropic Fermi surface. Interestingly, a very recent study demonstrated that (001) surfaces of TiO_2 thin films grown on STO have a (4×1) surface reconstruction, that can lead to partial gapping of the Fermi surface at sufficient doping [109]. Titanium d_{xy} -derived metallic subbands have additionally been reported on thin films of $\text{Sr}_{2-x}\text{La}_x\text{TiO}_4$ grown by molecular beam epitaxy and studied by *in situ* ARPES [110].

4. Coupling to the lattice

Several recent ARPES studies have identified signatures of electron-phonon coupling in STO surfaces and related systems. These works are important advances toward understanding superconductivity in bulk STO and STO-based heterostructures, as well as normal state transport in such systems. Beyond that, such research is opening new opportunities to test fundamental models within quantum many-body theory. Indeed, in STO and related systems, the ARPES signatures of polarons (mobile charge carriers dressed by co-propagating lattice polarizations) appear unusually clear and pronounced compared to other materials, such as manganites [111]. These polaronic features in STO repeatedly appear in the range of 80–100 meV, which corresponds with the highest energy longitudinal optical phonon branch. In addition, the doping of STO based systems can be tuned, bringing a crossover from the low-density limit favorable to polaron formation, to higher carrier density regimes where the screening is greater and the size of the Fermi surface may open scattering channels with finite momentum transfer.

Signatures of electron-phonon coupling were immediately reported in some of the first ARPES experiments on STO. In their initial study of lightly La-doped STO, Meevasana *et al* noted the appearance of dispersion ‘kinks’ (effective mass enhancements at sharply defined energy scales) at roughly 20 meV binding energy [76]. Additionally the authors found an overall band renormalization factor of about 1.7 compared to single-electron calculations using the local density

approximation (LDA), which they attributed to a broad spectrum of electron-phonon interactions with higher energy. King *et al* observed the same dispersion kinks in the d_{xy} bands of what was by that time recognized as the (001) surface state and calculated a slightly higher overall bandwidth renormalization factor of about 2.1 [105].

These results were somewhat different from ARPES spectra of the 3D bulk electron-doped state in high-temperature ($\sim 1000^\circ\text{C}$) vacuum annealed STO studied by Chang *et al* [20]. With such heavy annealing, the Fermi surface t_{2g} bands become quasi-degenerate, consistent with the symmetry of bulk STO. The authors observed ‘peak-dip-hump’ features in the ARPES energy distribution curves, rather than dispersion kinks. The spectral weight redistribution to the ‘hump’ at about 170 meV below E_F was interpreted as a spectroscopic signature of polaron formation in the lightly-doped bulk material. Later ARPES work by Chen *et al* investigated $\text{STO}(001)$ after vacuum annealing at temperatures ranging from 700°C , which leads to the widely-studied surface state [80], up to 1200°C , resulting in a 3D Fermi surface confirmed by k_z scans [112]. Polaron features seen in the quasi-2D system appeared to be reduced in the 3D state.

Anatase TiO_2 has also been found to display strong signatures of polarons. The in-depth analysis of the polaronic features in this system has served as a valuable stepping stone for a handful of later studies on STO and LAO/STO. Moser *et al* reported on ARPES measurements showing signatures of polarons formed in anatase TiO_2 thin films grown on STO, as well as Nb-doped bulk anatase TiO_2 crystals [113]. Similar to STO surfaces, carriers in TiO_2 were found to be induced by exposure to UV synchrotron radiation. In contrast to STO, however, the authors concluded that the k_z dispersion was consistent with a 3D electronic structure of the induced metallic state. By adjusting the beam intensity and oxygen background pressure during the ARPES experiments, Moser *et al* were able to tune the carrier density over a range of about 10^{18} – 10^{20} cm^{-3} . High binding energy tails consisting of replica bands scattered from the main band crossing E_F provided strong evidence of polarons in anatase TiO_2 . In energy distribution curves evaluated at the Fermi momentum k_F , the incoherent spectral weight of the replica bands could be fit with a Frank-Condon model using a single longitudinal optical (LO) phonon mode with an energy of 108 meV. The dispersion of the main band also showed significant electron mass enhancement (a factor of about 1.7 for $n = 5 \times 10^{18}\text{ cm}^{-3}$) compared to band structure calculations. With increasing carrier density, the incoherent part of the spectrum became more smeared while the coherent band also showed suppressed intensity near the Γ point.

Wang *et al* recently used a novel approach to achieve control over the carrier density of the $\text{STO}(001)$ surface state, which allowed the electron-phonon coupling to be studied by ARPES as a function of doping [68]. By performing a pretreatment of the sample surfaces using Ar^+ sputtering, followed by annealing at various temperatures (700 – 1000°C) in a low background pressure of oxygen ($2 \times 10^{-6}\text{ mbar}$), the surface state carrier density could be tuned by almost an order of magnitude from very low doping up to a saturated

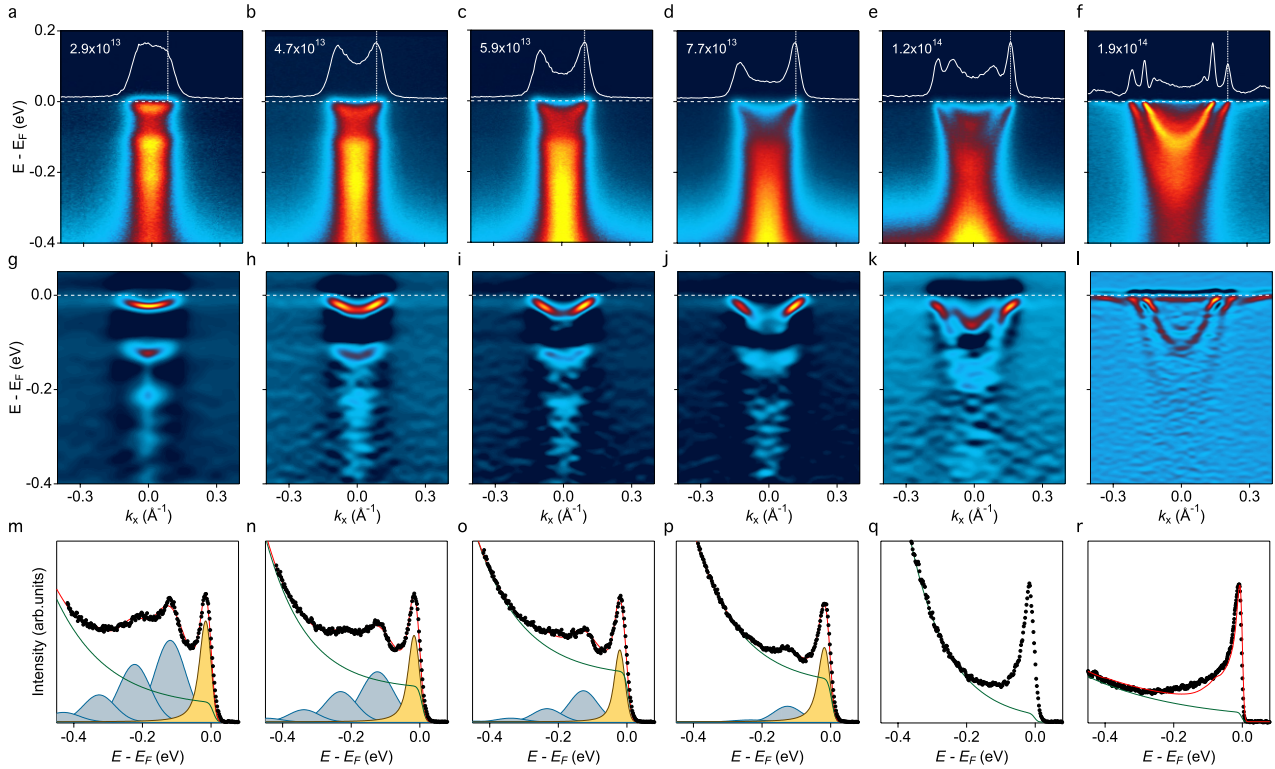


Figure 13. (a)–(f) ARPES spectra of the surface state on STO(001) acquired as a function of increasing carrier density. The images are cuts through the Γ point along (100) direction. The number on each panel is the 2D carrier density calculated from the Fermi surface size, assuming each band crossing the Fermi level is spin-degenerate. (g)–(l) The same spectra enhanced using the 2D curvature method [114] in order to clarify the replica bands. (m)–(r) Energy distribution curves evaluated at the Fermi momentum k_F of each corresponding image. The profiles in (g)–(j) are shown with fits of the main band and incoherent spectral tail to a Frank-Condon model with a single phonon mode of about 100 meV. Reprinted by permission from [68].

carrier density comparable to that seen in other ARPES measurements [77, 78, 80, 81]. The surfaces with relatively high carrier densities showed dispersion kinks in the d_{xy} bands, as previously reported [76, 81]. At lower carrier density, however, the authors found that a spectral tail forms below the main band (see figure 13). Image analysis showed that the tail was comprised of replica bands similar to those seen in TiO_2 and that the effective mass of the main band increased. Modeling of the ARPES spectral function was found to be consistent with coupling to a high-energy optical phonon mode having an energy of about 100 meV. From the systematic study of the effective mass and quasiparticle residue (essentially the coherent spectral weight in the system), Z , as a function of carrier density, the authors argued that the low-density spectral behavior reflects strong coupling at zero momentum transfer, consistent with the formation of long-range Fröhlich polarons. They furthermore identified two transition points, $n_1 \approx 4 \times 10^{13} \text{ cm}^{-2}$ and $n_2 \approx 9 \times 10^{13} \text{ cm}^{-2}$ characterizing the crossover from large polaron behavior exhibiting replica bands to a more Migdal-like coupling regime [115], typified by dispersion kinks, where the phonons are more effectively screened by the higher carrier density and the interaction energy scale is relatively small in relation to the occupied bandwidth.

Similar evidence of polarons was also recently found in a soft x-ray ARPES study of the LAO/STO interface. Analysis

by Cancellieri *et al* revealed scattered replicas of the d_{xz} and d_{yz} bands [116]. Based on the replica shift of ~ 118 meV, the features were attributed to coupling to a phonon mode on the highest optical branch (similar to bare STO and TiO_2). In a slight contrast to other reports, however, the authors argued that polarons in LAO/STO likely fit the criteria of the Holstein (short range), rather than Fröhlich (long range) polaron model.

Finally, though slightly outside the focus of this topical review, we briefly remark on new and spectacular developments in understanding the role of electron-phonon coupling at STO interfaces come from single unit cell FeSe grown on STO(001), which exhibits superconductivity up to ~ 100 K [117, 118]. Lee *et al* discovered replica bands below the hole-like and electron-like pockets at the Γ and M points of the Brillouin zone of the FeSe monolayer. Band replicas were observed at energies consistent with coupling to a single optical phonon mode with an energy of roughly 80 meV. The replicas were found to vanish as soon as an additional unit cell of FeSe was added. Both observations strongly implicate STO phonons coupling across the interface. The ratios of the main and replica peak intensities implied an electron-phonon coupling constant of $\lambda \sim 0.5$, and recent calculations have suggested that interfacial phonon coupling may account for a significant fraction of the T_c enhancement in single-unit-cell FeSe/STO [119].

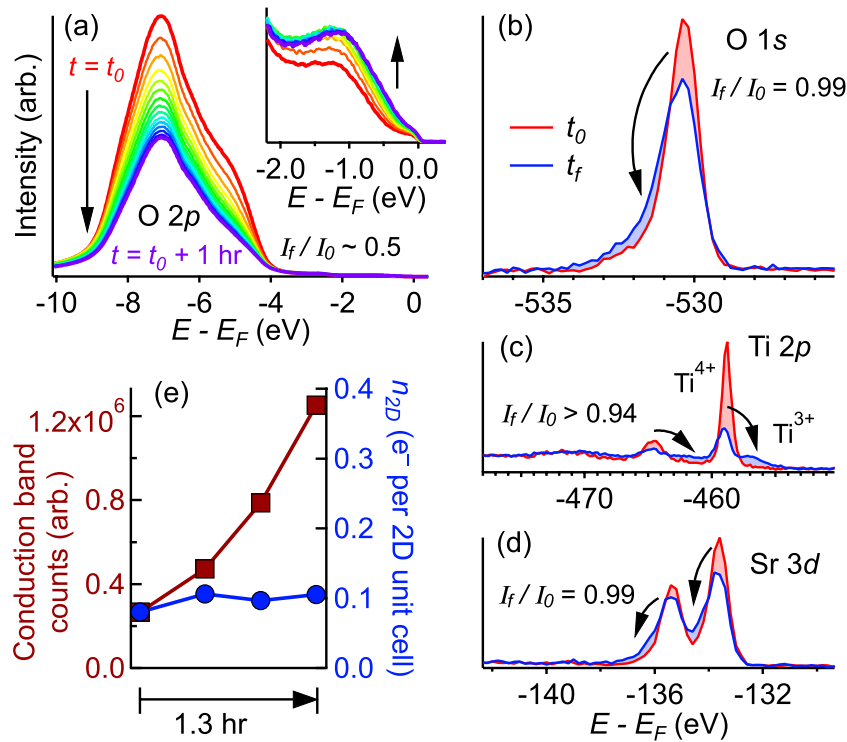


Figure 14. (a) Decrease in intensity from the O $2p$ valence band of STO during heavy irradiation with the synchrotron beam, along with simultaneous appearance of in-gap states at ~ 1 eV binding energy and counts at the Fermi energy (inset). (b)–(d) Redistribution of core level spectral weight from O $1s$, Ti $2p$, and Sr $3d$ during the same exposure. The ratio of each core level's total energy-integrated intensity before and after irradiation is shown (I_f/I_0). (e) Saturation of the Fermi surface volume (blue circles, right axis) in contrast to the continuously growing signal intensity from E_F (red squares, left axis). Reprinted with permission from [80]. Copyright (2014) by the American Physical Society.

5. Origins of surface/interface metallicity: roles of defects and photons

With some notable exceptions [112], groups studying STO [78, 80], KTaO_3 [105], CaTiO_3 [107], TiO_2 [108, 109, 113], and even LAO/STO [85] have reported that the metallic surface states of interest are formed and/or spectroscopically enhanced during exposure to the photon beam used for ARPES. In all cases, even those where metallic surface states were claimed to be insensitive to photon irradiation, the sample surfaces have been prepared in some manner—including scraping/fracturing, annealing, and/or ion sputtering—that will, by design, help to remove adsorbants and likely introduce any number of complicated defects or other changes to the systems. Thus, various ‘treatments’ are able to modify the metallic surface/interface states in question and in many cases may even be responsible for generating them. Understanding the relevant factors for altering these metallic states, as well as the mechanisms by which those factors operate, will be crucial for manipulating low-dimensional conducting states in order to probe their underlying physics and develop novel TMO devices.

Although there may be multiple ways that these surface states can be formed, the photo-induced mechanism appears particularly instructive for gaining insights into the factors that give rise to the surface metallicity, since the process can be readily monitored with respect to time and applied photon dose. Among those studies that observed photosensitivity of the surface state on STO(001), the phenomena listed below

and summarized in figure 14 appear to occur simultaneously while the sample is under irradiation. Under typical ARPES experimental conditions (ultrahigh vacuum, $T \sim 20$ K) the induced spectral changes are long-lived on the scale of many hours or even days after the beam has been turned off [80]. These behaviors are especially well-documented in the case of STO(001), but essentially the same phenomena have been noted on a number of other surface systems [104, 105, 108, 110, 120], as well as in LAO/STO interfaces [85]:

- decrease in intensity and changing shape of the O $2p$ valence band spectrum (figure 14(a));
- increase in intensity from in-gap states at roughly 1.3 eV binding energy (figure 14(a));
- rapid growth of the Fermi surface to a saturated size (carrier density of the 2D d_{xy} bands of $\sim \text{cm}^{-2}$);
- continued increase in photoemission intensity (at saturated Fermi surface size) from bands crossing E_F (figure 14(e));
- partial transfer of Ti core level spectral weight from Ti^{4+} peaks to nominal Ti^{3+} ‘shoulder’ features (figure 14(c)); the angular (in)dependence of the intensity of the Ti^{3+} shoulder indicates these states are rather tightly confined to the surface [80].

Further support indicating the importance of oxygen chemistry at the surface is noted based on the following:

- substantial increase in the rate of formation of the metallic state when the sample is irradiated with 52 eV, rather than

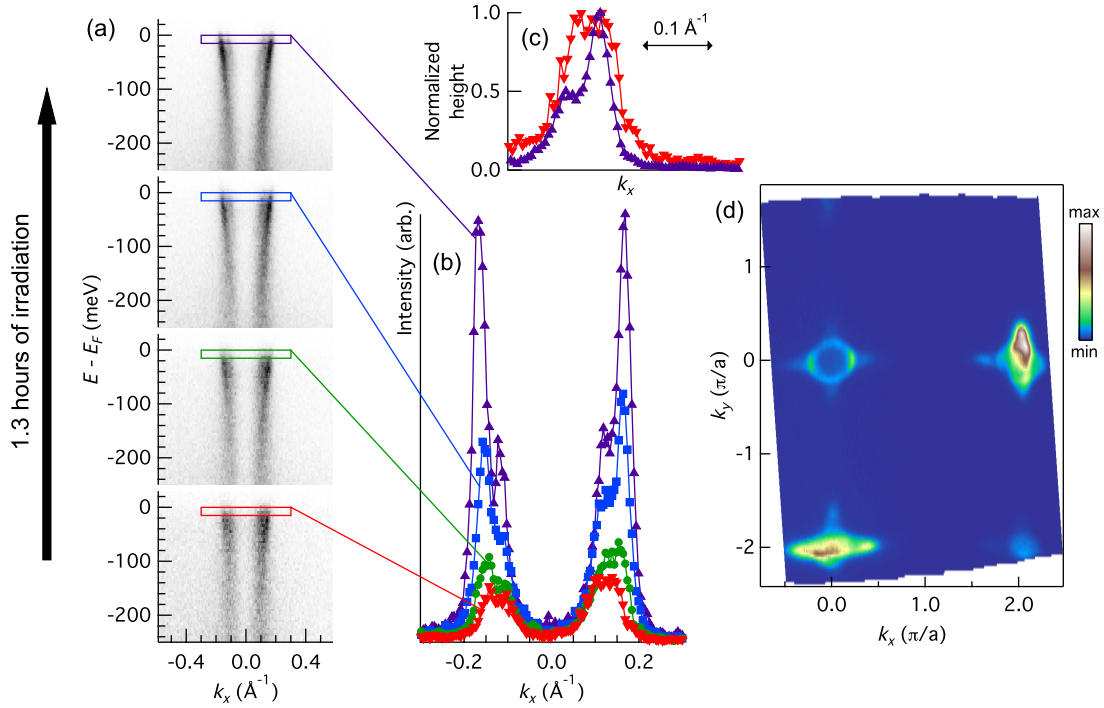


Figure 15. (a) ARPES measurements of the conduction band dispersion on STO(001) as a function of sample irradiation. The data were acquired in the first Brillouin zone using 47 eV circularly polarized photons, which shows the d_{xy} bands. The cuts are along the k_x direction with $k_y = 0$. (b) Momentum distribution curves evaluated near E_F over the course of irradiation. The Fermi momentum does not shift dramatically, even though there is a large increase in intensity and an improvement in the sharpness of the bands. (c) Normalized momentum distribution curves at the initial time and after 1.3 h of beam exposure. (d) Extended Fermi surface map showing the persistence of 1×1 order. The map was acquired with 85 eV circularly-polarized photons. Reprinted with permission from the supplemental material of [80].

28 eV, photons, which was argued to be consistent with a double-Auger process resulting in the release of O^+ [87];

- (g) reduction of the carrier density, or even vanishing of the metallic surface state and reversal of the coinciding signatures (a)–(e), after applying a low dose of oxygen to the surface [19, 103];
- (h) realization of the same surface band structure by deposition of Al, which reduces the surface of STO by the formation of aluminum oxides [121].

On the basis of all the above, there is no doubt that oxygen surface chemistry affects the existence and properties of the metallicity formed on the STO surface. Overall, the body of literature appears to be moving toward consensus that the surface states on STO and related oxides can essentially be explained solely on the grounds of oxygen vacancies.

Having said that, we would be remiss to not point out a number of unresolved issues, counterarguments, and even alternative scenarios. It would be prudent to conduct further experiments in order to put the oxygen vacancy consensus on even firmer footing. At a minimum, it is safe to say that the surface doping does not proceed straightforwardly in the sense of each missing O atom simply providing band bending and freeing two electrons into the conduction bands. More speculatively, there are additional factors and possible alternative sources of carriers to consider, which, even if they later come to be ruled out in the context of the the surface and interface states studied by ARPES so far, might still provide future pathways to realizing and manipulating metallicity

and other properties in STO-based and STO-like surfaces and interfaces.

To begin, we draw attention to a set of additional observations that should be considered alongside (a)–(h):

- (A) The loss in intensity of the O 2p valence band during irradiation, point (a), has been observed to reach as high as $\sim 50\%$, vastly larger than any observed change in the O 1s core level intensity under the same photon dose, which is at the single percent level [80].
- (B) Despite being widely referred to as an impurity band due to oxygen vacancies, recent density functional calculations including Coulomb interactions (DFT + U) found similar in-gap states due to Nb dopants, implying they are a *generic* spectroscopic signature of (trapped) doped electrons [122].
- (C) The saturated surface carrier density, point (c), does not correspond with any obvious limit, and it is unclear why the doping cannot proceed much further. From LEED and ARPES, the surface appears to remain 1×1 ordered (figure 15(d)); no reconstruction is observed that would signal, e.g. that oxygen vacancies organize into a stable ordered arrangement.
- (D) The saturated size of the Fermi surface is the same in many cases, despite drastically different annealing pre-treatments of the samples (e.g. in UHV or O_2) [77, 80].
- (E) During irradiation, the Sr 3d core level spectral weight partially redistributes to slightly ‘shoulder’-like features at deeper binding energy [80].

- (F) Surface x-ray diffraction experiments performed in air on STO(001) concluded that O atoms occupy the apical sites above the the surface Ti sites [123]. Thus, generally, one should consider that *excess* oxygen (or oxygen-containing species) may essentially be native to STO surfaces.
- (G) In cases of excessive vacuum annealing, the STO surface state appears to be lost [79] and gives way to a lightly-doped bulk state [20, 112]. Along these lines, Rödel *et al* have reported that photon irradiation on anatase TiO₂(001) leads to a gigantic loss of oxygen (verified by core level spectroscopy), which appears to destroy, rather than grow or enhance the Fermi surface [108]. We note the strong contrast to the behavior of STO(001) illustrated in figure 15, in which the Fermi surface intensifies and sharpens due to irradiation.

Observation (A) reveals that the amount of oxygen actually lost from the system due to irradiation is probably finite but much smaller than might be inferred from the valence band changes. Instead, the valence band lineshape and disproportionate intensity changes mentioned in point (a) hint at unknown but fundamental changes in the electrons' initial states, which are in turn presumably driven by subtle structural changes accompanying the presence of carriers. This might take the form, for instance, of buckling in the Ti–O and Sr–O intra-layers or some other restructuring of the surface. Given that the spectrum of the surface state sharpens over the course of irradiation (figure 15), the induced structure is presumably more ordered than the STO surface as it was originally prepared. Though the details are not yet understood, the general behavior underscores that the surface is being doped in a nontrivial manner involving the simultaneous evolution of the underlying electronic band structure. However this observation does not necessarily discredit O vacancies as the charge donors *per se*. Even a ~1% change reported in O 1s intensity (which some might consider to be below the trust threshold of XPS) is already close to accounting for the observed carrier density at the surface, if one assumes two electrons are freed to the conduction band as a result of each vacancy.

The saturation of the surface carrier density, point (C), further indicates the complexity of the process of forming the surface metal. The fact that the carrier density so quickly saturates while the photoemission signal at the Fermi level continues to intensify, (d), is consistent with the growth of a metallic region (or phase-mixed regions [124]) under the beam pinned to a uniform carrier density. Vacuum annealing also does not significantly increase the surface carrier density—in fact, over-annealing can kill the surface state [79]. Likewise the reducing process in (h) does not appear to lead to a larger Fermi surface. Finally, even more aggressive surface treatments using ion sputtering have not led to substantively higher surface doping [68]. While the factor(s) constraining the carrier density are still unresolved, the DFT + U study of Hao *et al* may offer a solution, by proposing that excess electrons above a critical doping become trapped by forming small polarons near defects. In their study, this behavior appears to be generic for doped STO and not depend on oxygen defects *per se*. Though trapped polarons are commonly

invoked to explain the existence of the in-gap states near 1 eV binding energy [125], a recent study has argued that they constitute a ‘Hubbard-like’ band derived from e_g states near oxygen vacancy sites that are subtly dressed by correlations [126].

The observed changes in the Sr 3d lineshape of point (E) may be signalling changes in Sr chemistry at the surface, such as migration or clustering of surface Sr [127]. This could be important to the physics of STO surfaces, since regions of excess Sr would, like O vacancies, donate electrons and promote downward band bending. Delugas *et al* recently reported on density functional theory (DFT) calculations wherein the stoichiometric SrO surface termination was found to confine carriers to the surface region, yielding a metallic surface state with Ti t_{2g} band structure similar to ARPES measurements [128]. On the other hand, while consideration of the A-site chemistry might extend to other ABO₃ formula systems (e.g. KTaO₃), it obviously cannot be invoked to explain the case of TiO₂.

Finally, point (F) is notable, because if some amount of excess oxygen is already present on the surfaces in question, it becomes difficult to prove that removed oxygen, e.g. as in point (h), truly takes the form of vacancies within STO. Rather, one might predominantly be removing oxygen adatoms. By this logic, the reversal of spectroscopic changes due to oxygen deposition, point (g), likewise does not constitute sound proof that O vacancies in the crystal are the sole deciding factor. Rather, oxygen may adsorb on top of the surface and even penetrate forming interstitial neutrals in to bulk and generically bring about the same effect of removing carriers from the surface state.

Another consideration in the formation of these surface and interface metallic states, aside from strontium migration or even possible adsorbates [129] on the surface, is the influence of ferroelectric-like surface/interface distortions. From general electrostatic principles, a discontinuity in electric displacement (related to polarization) is coupled to the existence of free charge. For this reason, ferroelectric domain walls or surfaces of poled ferroelectrics are expected to be metallic [130]. Given the (nearly) ferroelectric properties of STO and the confined regions of polar distortion at STO surfaces and interfaces (section 1.2.3), it is clear that the surface/interface polarization of these systems should not be neglected, as they would naturally be expected to influence virtually all properties of the conducting electrons, regardless of whether they originate from oxygen vacancies or other sources. Moreover, we believe it so far cannot be strictly ruled out that such systems might be, for all intents and purposes, intrinsically metallic once distorted regions are aligned in sufficiently large domains, which might be assisted, e.g. by photons [131, 132] and/or reduced partial pressure of oxygen [133].

6. Concluding remarks

Modern ARPES experiments have recently broken new ground in the field of conducting states realized at TMO surfaces and interfaces by giving a unique and direct momentum-space view into the electronic, orbital, and spin structure of these

systems. As general templates for engineering low-dimensional metallic states in oxides, ARPES results show that STO and STO-like surfaces and interfaces are quite closely related, consisting of occupied t_{2g} conduction bands, but can nevertheless take on different orbital characters and 2D/3D characteristics depending, e.g. on the particular compound and surface/interface orientation. Photoemission experiments also find clear signatures of strong electron-phonon interactions, which can likewise be tuned by doping and dimensionality, offering opportunities for testing quantum many-body theories, as well as promising routes for better understanding superconductivity—not only in STO but also, e.g. in single unit cell FeSe/STO. ARPES studies are furthermore giving unique insights into the origins of metallicity in these systems and ways in which their properties might be tuned by external factors such as photons and/or defects. Meanwhile opportunities exist for further exploration into unresolved issues surrounding the spin structure and magnetic properties of conducting TMO surfaces and interfaces, which could help extend their potential applications into the realm of spintronics. Thus we emphasize that information gained from ARPES studies on these systems can help advance next-generation multi-functional oxide-based technologies, as well as fundamental investigations into the complex physics of oxide materials.

Acknowledgments

The authors are indebted to J H Dil, Z Wang, C Cancellieri, S Muff, T Schmitt, and S Johnston for useful discussions and feedback in the preparation of this manuscript.

ORCID iDs

Nicholas C Plumb  <https://orcid.org/0000-0002-2334-8494>

References

- [1] Ohtomo A and Hwang H Y 2004 *Nature* **427** 423–6
- [2] Hotta Y, Susaki T and Hwang H Y 2007 *Phys. Rev. Lett.* **99** 236805
- [3] Perna P *et al* 2010 *Appl. Phys. Lett.* **97** 152111
- [4] Di Gennaro E *et al* 2013 *Adv. Opt. Mater.* **1** 834–43
- [5] Chen G and Balents L 2013 *Phys. Rev. Lett.* **110** 206401
- [6] Lytle F W 1964 *J. Appl. Phys.* **35** 2212–5
- [7] Salman Z *et al* 2006 *Phys. Rev. Lett.* **96** 147601
- [8] Salman Z, Smadella M, MacFarlane W A, Patterson B D, Willmott P R, Chow K H, Hossain M D, Saadaoui H, Wang D and Kie R F 2011 *Phys. Rev. B* **83** 224112
- [9] Kubo T and Nozoye H 2003 *Surf. Sci.* **542** 177–91
- [10] Erdman N, Poeppelmeier K R, Asta M, Warschkow O, Ellis D E and Marks L D 2002 *Nature* **419** 55–8
- [11] Herger R, Willmott P R, Bunk O, Schlepütz C M, Patterson B D, Delley B, Shneerson V L, Lyman P F and Saldin D K 2007 *Phys. Rev. B* **76** 195435
- [12] Herger R, Willmott P R, Bunk O, Schlepütz C M, Patterson B D and Delley B 2007 *Phys. Rev. Lett.* **98** 076102
- [13] Kawasaki M, Takahashi K, Maeda T, Tsuchiya R, Shinohara M, Ishiyama O, Yonezawa T, Yoshimoto M and Koinuma H 1994 *Science* **266** 1540–2
- [14] Koster G, Kropman B L, Rijnders G J H M, Blank D H A and Rogalla H 1998 *Appl. Phys. Lett.* **73** 2920–2
- [15] Kareev M, Prosandeev S, Liu J, Gan C, Kareev A, Freeland J W, Xiao M and Chakhalian J 2008 *Appl. Phys. Lett.* **93** 061909
- [16] Connell J G, Isaac B J, Ekanayake G B, Strachan D R and Seo S S A 2012 *Appl. Phys. Lett.* **101** 251607
- [17] van Benthem K, Elsasser C and French R H 2001 *J. Appl. Phys.* **90** 6156–64
- [18] Mattheiss L F 1972 *Phys. Rev. B* **6** 4718–40
- [19] Aiura Y, Hase I, Bando H, Yasue T, Saitoh T and Dessau D S 2002 *Surf. Sci.* **515** 61–74
- [20] Chang Y J, Bostwick A, Kim Y S, Horn K and Rotenberg E 2010 *Phys. Rev. B* **81** 235109
- [21] Popović Z S, Satpathy S and Martin R M 2008 *Phys. Rev. Lett.* **101** 256801
- [22] Caviglia A D, Gabay M, Gariglio S, Reyren N, Cancellieri C and Triscone J M 2010 *Phys. Rev. Lett.* **104** 126803
- [23] Thiel S, Hammerl G, Schmehl A, Schneider C W and Mannhart J 2006 *Science* **313** 1942–5
- [24] Schlom D G and Mannhart J 2011 *Nat. Mater.* **10** 168–9
- [25] Herranz G, Sánchez F, Dix N, Scigaj M and Fontcuberta J 2012 *Sci. Rep.* **2** 758
- [26] Schooley J F, Hosler W R and Cohen M L 1964 *Phys. Rev. Lett.* **12** 474–5
- [27] Koonce C S, Cohen M L, Schooley J F, Hosler W R and Pfeiffer E R 1967 *Phys. Rev.* **163** 380–90
- [28] Bardeen J, Cooper L N and Schrieffer J R 1957 *Phys. Rev.* **108** 1175–204
- [29] Reyren N *et al* 2007 *Science* **317** 1196–9
- [30] Bert J A *et al* 2012 *Phys. Rev. B* **86** 060503
- [31] Richter C *et al* 2013 *Nature* **502** 528–31
- [32] Edge J M, Kedem Y, Aschauer U, Spaldin N A and Balatsky A V 2015 *Phys. Rev. Lett.* **115** 247002
- [33] Müller K A and Burkard H 1979 *Phys. Rev. B* **19** 3593–602
- [34] Wemple S H 1965 *Phys. Rev.* **137** A1575–82
- [35] Bednorz J G and Müller K A 1984 *Phys. Rev. Lett.* **52** 2289–92
- [36] Itoh M, Wang R, Inaguma Y, Yamaguchi T, Shan Y J and Nakamura T 1999 *Phys. Rev. Lett.* **82** 3540–3
- [37] Jang H W *et al* 2010 *Phys. Rev. Lett.* **104** 197601
- [38] Haeni J H *et al* 2004 *Nature* **430** 758–61
- [39] Cohen R E 1992 *Nature* **358** 136–8
- [40] Choudhury D, Pal B, Sharma A, Bhat S V and Sarma D D 2013 *Sci. Rep.* **3** 1433
- [41] Ikeda A, Nishimura T, Morishita T and Kido Y 1999 *Surf. Sci.* **433–5** 520–4
- [42] Hikita T, Hanada T, Kudo M and Kawai M 1993 *Surf. Sci.* **287–8** 377–81
- [43] van der Heide P, Jiang Q, Kim Y and Rabalais J 2001 *Surf. Sci.* **473** 59–70
- [44] Heifets E, Eglitis R I, Kotomin E A, Maier J and Borstel G 2001 *Phys. Rev. B* **64** 235417
- [45] Pauli S A, Leake S J, Delley B, Björck M, Schneider C W, Schlepütz C M, Martocchia D, Paetel S, Mannhart J and Willmott P R 2011 *Phys. Rev. Lett.* **106** 036101
- [46] Cantoni C *et al* 2012 *Adv. Mater.* **24** 3952–7
- [47] Salluzzo M, Gariglio S, Torrelles X, Ristic Z, Di Capua R, Drnec J, Sala M M, Ghiringhelli G, Felici R and Brookes N B 2013 *Adv. Mater.* **25** 2333–8
- [48] Rice W D, Ambwani P, Bombeck M, Thompson J D, Haugstad G, Leighton C and Crooker S A 2014 *Nat. Mater.* **13** 481–7
- [49] Rao S S, Lee Y F, Prater J T, Smirnov A I and Narayan J 2014 *Appl. Phys. Lett.* **105** 042403
- [50] Liu Z Q *et al* 2013 *Phys. Rev. B* **87** 220405
- [51] Brinkman A, Huijben M, van Zalk M, Huijben J, Zeitler U, Maan J C, van der Wiel W G, Rijnders G, Blank D H A and Hilgenkamp H 2007 *Nat. Mater.* **6** 493–6

- [52] Bert J A, Kalisky B, Bell C, Kim M, Hikita Y, Hwang H Y and Moler K A 2011 *Nat. Phys.* **7** 767–71
- [53] Pentcheva R and Pickett W E 2006 *Phys. Rev. B* **74** 035112
- [54] Banerjee S, Erten O and Randeria M 2013 *Nat. Phys.* **9** 626–30
- [55] Chen Y Z *et al* 2013 *Nat. Commun.* **4** 1371
- [56] Gor'kov L P 2015 *J. Phys.: Condens. Matter* **27** 252001
- [57] Lee J S, Xie Y W, Sato H K, Bell C, Hikita Y, Hwang H Y and Kao C C 2013 *Nat. Mater.* **12** 703–6
- [58] Salluzzo M *et al* 2013 *Phys. Rev. Lett.* **111** 087204
- [59] Damascelli A, Hussain Z and Shen Z X 2003 *Rev. Mod. Phys.* **75** 473–541
- [60] Damascelli A 2004 *Phys. Scr. T* **109** 61
- [61] Hüfner S 2003 *Photoelectron Spectroscopy: Principles and Applications* 3rd edn (Berlin: Springer)
- [62] Dil J H 2009 *J. Phys.: Condens. Matter* **21** 403001
- [63] Cao Y *et al* 2012 arXiv:1211.5998
- [64] Zhu Z H *et al* 2014 *Phys. Rev. Lett.* **112** 076802
- [65] Kuroda K, Yaji K, Nakayama M, Harasawa A, Ishida Y, Watanabe S, Chen C T, Kondo T, Komori F and Shin S 2016 *Phys. Rev. B* **94** 165162
- [66] Seah M P and Dench W A 1979 *Surf. Interface Anal.* **1** 2–11
- [67] Hatch R C, Fredrickson K D, Choi M, Lin C, Seo H, Posadas A B and Demkov A A 2013 *J. Appl. Phys.* **114** 103710
- [68] Wang Z *et al* 2016 *Nat. Mater.* **15** 835–9
- [69] Fujishima A and Honda K 1972 *Nature* **238** 37–8
- [70] Ohashi K, McCann J and Bockris J O 1977 *Nature* **266** 610–1
- [71] Morin F J and Wolfram T 1973 *Phys. Rev. Lett.* **30** 1214–7
- [72] Ellialtıoğlu Ş and Wolfram T 1978 *Phys. Rev. B* **18** 4509–25
- [73] Ellialtıoğlu Ş, Wolfram T and Henrich V E 1978 *Solid State Commun.* **27** 321–4
- [74] Henrich V E, Dresselhaus G and Zeiger H J 1978 *Phys. Rev. B* **17** 4908–21
- [75] Courths R, Cord B and Saalfeld H 1989 *Solid State Commun.* **70** 1047–51
- [76] Meevasana W *et al* 2010 *New J. Phys.* **12** 023004
- [77] Santander-Syro A F *et al* 2011 *Nature* **469** 189–93
- [78] Meevasana W, King P D C, He R H, Mo S K, Hashimoto M, Tamai A, Songsiririthigul P, Baumberger F and Shen Z X 2011 *Nat. Mater.* **10** 114–8
- [79] Di Capua R *et al* 2012 *Phys. Rev. B* **86** 155425
- [80] Plumb N C *et al* 2014 *Phys. Rev. Lett.* **113** 086801
- [81] King P D C *et al* 2014 *Nat. Commun.* **5** 3414
- [82] Stengel M 2011 *Phys. Rev. Lett.* **106** 136803
- [83] Ohta T, Bostwick A, McChesney J L, Seyller T, Horn K and Rotenberg E 2007 *Phys. Rev. Lett.* **98** 206802
- [84] Petrović A P, Paré A, Paudel T R, Lee K, Holmes S, Barnes C H W, David A, Wu T, Tsybal E Y and Panagopoulos C 2014 *Sci. Rep.* **4** 5338
- [85] Plumb N C *et al* 2017 *Appl. Surf. Sci.* **412** 271–8
- [86] Chang Y J, Moreschini L, Bostwick A, Gaines G A, Kim Y S, Walter A L, Freelon B, Tebano A, Horn K and Rotenberg E 2013 *Phys. Rev. Lett.* **111** 126401
- [87] Walker S M *et al* 2015 *Adv. Mater.* **27** 3894–9
- [88] Rashba E I 1960 *Sov. Phys.—Solid State* **2** 1109
- [89] Bychkov Y A and Rashba E I 1984 *J. Phys. C: Solid State Phys.* **17** 6039
- [90] Santander-Syro A F, Fortuna F, Bareille C, Rödel T C, Landolt G, Plumb N C, Dil J H and Radović M 2014 *Nat. Mater.* **13** 1085–90
- [91] Bihlmayer G, Blügel S and Chulkov E V 2007 *Phys. Rev. B* **75** 195414
- [92] Gierz I, Stadtmüller B, Vuorinen J, Lindroos M, Meier F, Dil J H, Kern K and Ast C R 2010 *Phys. Rev. B* **81** 245430
- [93] Coey J M D, Venkatesan M and Stamenov P 2016 *J. Phys.: Condens. Matter* **28** 485001
- [94] Kalisky B, Bert J A, Klopfer B B, Bell C, Sato H K, Hosoda M, Hikita Y, Hwang H Y and Moler K A 2012 *Nat. Commun.* **3** 922
- [95] Salman Z *et al* 2012 *Phys. Rev. Lett.* **109** 257207
- [96] Pavlenko N, Kopp T, Tsybal E Y, Mannhart J and Sawatzky G A 2012 *Phys. Rev. B* **86** 064431
- [97] Walker S M *et al* 2016 *Phys. Rev. B* **93** 245143
- [98] Berner G *et al* 2010 *Phys. Rev. B* **82** 241405
- [99] Cancellieri C, Reinle-Schmitt M L, Kobayashi M, Strocov V N, Willmott P R, Fontaine D, Ghosez P, Filippetti A, Delugas P and Fiorentini V 2014 *Phys. Rev. B* **89** 121412
- [100] Ament L J P, van Veenendaal M, Devereaux T P, Hill J P and van den Brink J 2011 *Rev. Mod. Phys.* **83** 705–67
- [101] Zhou K J, Radovic M, Schlappa J, Strocov V, Frison R, Mesot J, Patthey L and Schmitt T 2011 *Phys. Rev. B* **83** 201402
- [102] Rödel T C *et al* 2014 *Phys. Rev. Appl.* **1** 051002
- [103] Walker S M, de la Torre A, Bruno F Y, Tamai A, Kim T K, Hoesch M, Shi M, Bahramy M S, King P D C and Baumberger F 2014 *Phys. Rev. Lett.* **113** 177601
- [104] Wang Z *et al* 2014 *Proc. Natl Acad. Sci. USA* **111** 3933–7
- [105] King P D C *et al* 2012 *Phys. Rev. Lett.* **108** 117602
- [106] Bareille C *et al* 2014 *Sci. Rep.* **4** 3586
- [107] Muff S, Fanciulli M, Weber A P, Pilet N, Ristić Z, Wang Z, Plumb N C, Radović M and Dil J H 2017 *Appl. Surf. Sci.* <https://doi.org/10.1016/j.apsusc.2017.05.229> (advanced online publication)
- [108] Rödel T C, Fortuna F, Bertran F, Gabay M, Rozenberg M J, Santander-Syro A F and Le Fèvre P 2015 *Phys. Rev. B* **92** 041106
- [109] Wang Z *et al* 2017 *Nano Lett.* **17** 2561–7
- [110] Nie Y F, Di Sante D, Chatterjee S, King P D C, Uchida M, Ciuchi S, Schlom D G and Shen K M 2015 *Phys. Rev. Lett.* **115** 096405
- [111] Mannella N, Yang W L, Zhou X J, Zheng H, Mitchell J F, Zaanen J, Devereaux T P, Nagaosa N, Hussain Z and Shen Z X 2005 *Nature* **438** 474–8
- [112] Chen C, Avila J, Frantzeskakis E, Levy A and Asensio M C 2015 *Nat. Commun.* **6** 8585
- [113] Moser S *et al* 2013 *Phys. Rev. Lett.* **110** 196403
- [114] Zhang P, Richard P, Qian T, Xu Y M, Dai X and Ding H 2011 *Rev. Sci. Instrum.* **82** 043712
- [115] Mahan G D 2000 *Many-Particle Physics* 3rd edn (New York: Plenum)
- [116] Cancellieri C, Mishchenko A S, Aschauer U, Filippetti A, Faber C, Barisic O S, Rogalev V A, Schmitt T, Nagaosa N and Strocov V N 2016 *Nat. Commun.* **7** 10386
- [117] Wang Q Y *et al* 2012 *Chin. Phys. Lett.* **29** 037402
- [118] Ge J F, Liu Z L, Liu C, Gao C L, Qian D, Xue Q K, Liu Y and Jia J F 2015 *Nat. Mater.* **14** 285–9
- [119] Rademaker L, Wang Y, Berlijn T and Johnston S 2016 *New J. Phys.* **18** 022001
- [120] Masingboon C, Eknapakul T, Suwanwong S, Buaphet P, Nakajima H, Mo S K, Thongbai P, King P D C, Maensiri S and Meevasana W 2013 *Appl. Phys. Lett.* **102** 202903
- [121] Rödel T C *et al* 2016 *Adv. Mater.* **28** 1976–80
- [122] Hao X, Wang Z, Schmid M, Diebold U and Franchini C 2015 *Phys. Rev. B* **91** 085204
- [123] Vonk V, Konings S, van Hummel G, Harkema S and Graafsma H 2005 *Surf. Sci.* **595** 183–93
- [124] Dudy L, Sing M, Scheiderer P, Denlinger J D, Schtz P, Gabel J, Buchwald M, Schlueter C, Lee T L and Claessen R 2016 *Adv. Mater.* **28** 7443–9
- [125] Janotti A, Varley J B, Choi M and Van de Walle C G 2014 *Phys. Rev. B* **90** 085202
- [126] Lechermann F, Jeschke H O, Kim A J, Backes S and Valentí R 2016 *Phys. Rev. B* **93** 121103

- [127] Kobayashi D, Kumigashira H, Oshima M, Ohnishi T, Lippmaa M, Ono K, Kawasaki M and Koinuma H 2004 *J. Appl. Phys.* **96** 7183–8
- [128] Delugas P, Fiorentini V, Mattoni A and Filippetti A 2015 *Phys. Rev. B* **91** 115315
- [129] D’Angelo M, Yukawa R, Ozawa K, Yamamoto S, Hirahara T, Hasegawa S, Silly M G, Sirotti F and Matsuda I 2012 *Phys. Rev. Lett.* **108** 116802
- [130] Fechner M, Ostanin S and Mertig I 2008 *Phys. Rev. B* **77** 094112
- [131] Nozawa S, Iwazumi T and Osawa H 2005 *Phys. Rev. B* **72** 121101
- [132] Qiu Y, Nasu K and Wu C Q 2007 *Phys. Rev. B* **75** 064103
- [133] Highland M J, Fister T T, Fong D D, Fuoss P H, Thompson C, Eastman J A, Streiffer S K and Stephenson G B 2011 *Phys. Rev. Lett.* **107** 187602